# CHAPTER 2

## $Li^+$-induced Fluorescent Metallogel

## 2.1 INTRODUCTION

Chelation enhanced fluorescence (CHEF) is usually obtained by coordination/chelation of metal ion with ligand having lone pairs. Chelation enhanced fluorescence (CHEF)[1] and intra-molecular charge transfer (ICT)[2] phenomena triggered by metal ions have been widely utilized in the fields of sensing, aggregation and biological imaging, but rarely applied in the case of metallogels. In general, CHEF is introduced in ligands using traditional moieties such as terpyridyl, amides or high molecular weight ligands based on the porphyrin moiety.[1-3] Utilizing the concepts of CHEF and ICT, we recently reported two chiral metallogels based on L-tartaric acid derived symmetrical gelators.[4,5] Therein, we explored that the metal binding to the ligand enroots the appearance of fluorescence (CHEF) as well as a conformational change which provides a planar platform for π–π stacking leading to aggregation followed by gelation. Further, the metallogel also showed interesting nanocluster morphology and optical and rheological properties.[4] In the present chapter, we would deduce the effect of removal of middle flexible chiral tartaric core with rigid hydrazine core over fluorescence and morphological properties (Scheme 2.1). Taking all this into consideration, in this chapter, we described the synthesis of a metallogel obtained from the lowest possible symmetrical aromatic ligand and LiOH as well the explored the fluorescence phenomenon involved in mechanism of gelation.

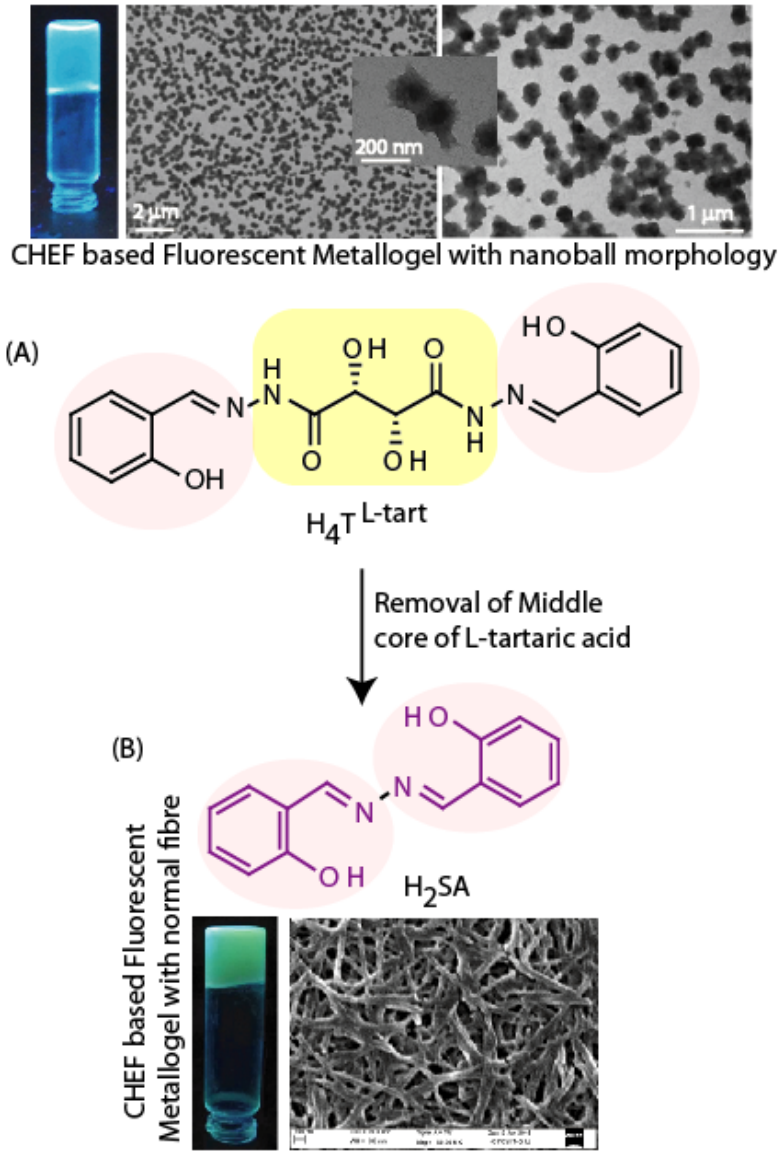


**Scheme 2.1** A schematic presentation of origin of idea towards designing of $H_2SA$ from our previous works. (A) L-tartaric acid derived $H_4T^{-L\text{-}tart}$ ligand produces fluorescent metallogel upon LiOH addition and exhibited exceptional nanoball morphology and (B) Removal of middle chiral tartaric core form $H_4T^{-L\text{-}tart}$ leads to ligand $H_2SA$ which also produces fluorescent metallogel with long range fibrous morphology. [4]–Reproduced by permission of The Royal Society of Chemistry

## 2.2 EXPERIMENTAL METHODS

### 2.2.1 Materials and physical methods

The solvents were distilled and dried by standard procedures prior to their use. Reagents and solvents used in experiments were purchased from Avra Synthesis Pvt. Ltd, Merck

Specialties Private Limited and S. D. Fine Chem. Ltd, Mumbai, India and used as received without further purification. Salicylaldehyde, *m*-hydroxy benzaldehyde, *p*-hydroxy benzaldehyde, *p*-methoxy benzaldehyde and *p*-phenylenediamine were purchased from Avra Synthesis Pvt. Ltd, Hyderabad, India. Hydrazine mono-hydrate and ethylene diamine were purchased from Merck Specialties Private Limited and S. D. Fine Chem. Ltd, Mumbai, India respectively. All the compounds were synthesized by slight modification of the literature procedures. [6–10] Elemental analyses were acquired on an Exeter CHN Analyzer CE-440. FT IR and UV-vis studies of ligands, dried solutions and xerogels were done using a PerkinElmer Spectrum Two and a Thermo Scientific EVOLUTION 200 spectrophotometer, respectively. Photoluminescence spectra were acquired on a PerkinElmer LS 55 spectrophotometer. The lifetime measurements were made using a time-correlated single photon counting (TCSPC) system from Horiba Yovin (Model: Delta Flex) and data analysis was performed using EzTime (HORIBA Scientific) decay analysis software. SEM images were captured by Carl Zeiss EVO/ 18 Research 2045 and Oxford Instruments 5IN1000EDS. Powder XRD data was collected using RigakuSmartLab between angle $2\theta$ = 10°–40°. $^{1}$H NMR spectra were obtained on a Bruker AVANCE III HD 500 spectrometer.

### 2.2.2 X-ray crystallography

Single crystals of $C_7H_7NO$ ($H_2SA$) were obtained from the reaction mixture of **$H_2SA$** (chloroform) with CsOH (methanol). A suitable crystal was selected and mounted on glass fiber on a SuperNova, Single source at offset/far, HyPix3000 diffractometer. The crystal was kept at 293 K during data collection. Using Olex2 the structure was solved with the ShelXT structure solution program using Intrinsic Phasing and refined with the olex2.refine refinement package using Gauss–Newton minimization. [11–13]

### 2.2.3 Rheological study

Measurements were performed using a stress-controlled Rheometer (Anton Paar TWINE Rheometer MCR 702) equipped with stainless steel parallel plates (20 mm diameter, 1.0 mm gap). Experiments were carried out on freshly prepared gels (1% w/v). Linear viscoelastic regions of the gel samples were determined by measuring the storage modulus, G' (associated with energy storage) and the loss modulus, G" (associated with the loss of energy) as a function of stress amplitude (dynamic oscillatory frequency of 1 rad $s^{-1}$). The following tests were performed: increasing amplitude of oscillation up to 100% apparent strain on shear, time and frequency sweeps at 20 $^oC$ (20 min and from 0.1 to 100 rad $s^{-1}$, respectively) and a heating run to 90 $^oC$ at a scan rate of 5 $^oC$ $min^{-1}$. All these measurements were conducted in triplicate.

### 2.2.4 Lifetime measurements

The lifetime measurements were made using a time-correlated single photon counting (TCSPC) system from Horiba Yovin (Model: Delta Flex). 1/$Li^+$ ($CHCl_3$/MeOH, 1x$10^{-3}$ M), 1/$Na^+$ ($CHCl_3$/MeOH, 1x$10^{-3}$ M), 2/$Li^+$ ($CHCl_3$: DMSO (4:1) /MeOH, 1x$10^{-3}$ M) and 6/$Li^+$ ($CHCl_3$/MeOH, 1x$10^{-3}$ M) were excited at 363 nm, 323 nm and 370 nm, respectively, using a picosecond diode laser (Model: Delta Diode) and data analysis was performed using EzTime (HORIBA Scientific) decay analysis software. Following equation 2.1 is used to calculate average lifetime value,

$$\tau_{(av)} = \frac{(\alpha_1.\tau_1) + (\alpha_2.\tau_2) + (\alpha_3.\tau_3)}{(\alpha_1+\alpha_2+\alpha_3)} \quad \text{Equation 2.1}$$

where, $\tau_{(av)}$ is average lifetime, $\tau_1$, $\tau_2$, $\tau_3$ are decay components and $\alpha_1$, $\alpha_2$, $\alpha_3$ are respective amplitudes.

### 2.2.5 Synthetic procedure

**2.2.5.1 Salicylaldehydeazine or [bis-(2-hydroxybenzylidene)-hydrazine] ($H_2SA$)**. A methanolic solution of 2-hydroxybenzaldehyde (0.501 g, 3.10 mmol) was added drop wise to a solution of hydrazine monohydrate (0.100 g, 2.05 mmol) in methanol and the resulting solution was refluxed for 10–15 min and then stirred for 4–6 hours at room temperature to complete the reaction. It afforded a yellow crystalline compound which was washed with methanol, hexane and diethyl ether and dried under vacuum. Yield 0.400 g (87%). Anal. *calcd* for $C_{14}H_{12}N_2O_2$: C, 69.99; H, 5.03; N, 11.66. Found C, 69.87; H, 5.11; N, 11.73. $^1$H NMR ($CDCl_3$, 500 MHz, $\delta_H$, ppm) 6.952 (t, 2H, Ar), 7.0 (d, 2H, Ar), 7.3 (d, 2H, Ar), 7.4 (t, 2H, Ar), 8.7 (s, 2H, =CH) and 11.4 (s, 2H, –OH). *m/z*, ESI-MS: $[M + H]^+$, 241.09 (*calcd* 241.09). Liquid state IR ($CHCl_3$, $cm^{-1}$) $\nu(C=N)_{stretch}$ 1618. UV-vis spectrum (chloroform) [$\lambda$, nm ($\varepsilon$, $M^{-1}cm^{-1}$)]: 295 (25 800), 363 (20 700).

**2.2.5.2 Bis(4-hydroxybenzylidene)hydrazine ($H_2PBA$).** A methanolic solution of 4-hydroxybenzaldehyde (0.501 g, 3.10 mmol) was added drop wise to a solution of hydrazine monohydrate (0.100 g, 2.05 mmol) in methanol and the resulting solution was stirred for 4–6 hours to complete the reaction. It afforded a yellow precipitate by *in vacuo* solvent removal which was washed with hexane and diethyl ether and dried under vacuum. Yield 0.377 g (83%). Anal. *calcd* for $C_{14}H_{12}N_2O_2$: C, 69.99; H, 5.03; N, 11.66. Found C, 70.11; H, 5.07; N, 11.33. $^1$H NMR (DMSO-$d_6$, 500 MHz, $\delta_H$, ppm) 6.8 (d, 2H, Ar), 7.7 (d, 2H, Ar), 8.5 (s, 2H, =CH). *m/z,* ESI-MS: $[M + H]^+$, 241.09 (*calcd* 241.09). Liquid state IR ($CHCl_3$/DMSO, $cm^{-1}$), $\nu_{as}(C=N)_{stretch}$ 1606. UV-vis spectrum ($CHCl_3$/DMSO, 4:1) [$\lambda$, nm ($\varepsilon$, $M^{-1}cm^{-1}$)]: 323 (19 800).

**2.2.5.3 Bis(3-hydroxybenzylidene)hydrazine ($H_2$MBA).** Methanolic solution of 3-hydroxybenzaldehyde (0.501 g, 3.10 mmol) was added drop wise to a solution of hydrazine (0.100 g, 2.05 mmol) in methanol and the resulting solution was stirred for 4–6 hours to complete the reaction. Then, this reaction mixture was filtrated and kept for crystallization. It afforded shiny yellow crystals in 24 h which were washed with chloroform and ether and dried under vacuum. Yield 240 mg (82%). Anal. *calcd* for $C_{14}H_{12}N_2O_2$: C, 69.99; H, 5.03; N, 11.66. Found C, 70.14; H, 3.99; N, 11.39. $^1$H NMR ($CDCl_3$, 500 MHz, $\delta_H$, ppm) 6.9 (d, 2H, Ar), 7.3(m, 6H, Ar), 8.6 (s, 2H, =CH), 9.7 (s, 2H, –OH). *m/z*, ESI-MS: $[M+H]^+$, 241.09 (*calcd* 241.09). Liquid state IR ($CHCl_3$, cm $^1$) $\nu_{as}(C=N)_{stretch}$ 1666. UV-vis spectrum ($CHCl_3$) [$\lambda$, nm ($\varepsilon$, $M^{-1}cm^{-1}$)]: 303 nm (18 300).

**2.2.5.4 N,N'-Bis(4-methoxybenzylidene)hydrazine (PMO).** A methanolic solution of 4-methoxybenzaldehyde (0.557 g, 3.10 mmol) was added drop wise to a solution of hydrazine (0.100 g, 2.05 mmol) in methanol and the resulting solution was stirred for 4–6 hours to complete the reaction. It afforded a yellow compound which was washed with methanol, hexane and diethyl ether and dried under vacuum. Yield 0.423 g (79%). Anal. *calcd* for $C_{14}H_{12}N_2O_2$: C, 71.62; H, 6.01; N, 10.43. Found C, 71.24; H, 5.98; N, 10.37. $^1$H NMR ($CDCl_3$, 500 MHz, $\delta_H$, ppm) 3.8 (s, 6H, $–CH_3$), 6.9 (d, 4H, Ar), 7.7 (d, 4H, Ar), 8.6 (s, 2H, =CH). *m/z*, ESI-MS: $[M + H]^+$, 269.013 (*calcd* 269.13). Liquid state IR ($CHCl_3$, $cm^{-1}$) $\nu_{as}(C=N)_{stretch}$ 1666. UV-vis spectrum ($CHCl_3$) [$\lambda$, nm ($\varepsilon$, $M^{-1}cm^{-1}$)]: 330 (19 500).

**2.2.5.5 N,N'-Bis(salicylidene)ethylenediamine ($H_2$SEA).** A methanolic solution of 2-hydroxybenzaldehyde (0.488 g, 4 mmol) was added drop wise to a solution of ethylene diamine (0.120 g, 2 mmol) in methanol and the resulting solution was stirred for 4–6 hours to complete the reaction. It afforded a shiny yellow compound which was washed with

methanol, hexane and diethyl ether and dried under vacuum. Yield 0.334 g (83%). Anal. *calcd* for $C_{14}H_{12}N_2O_2$: C, 71.62; H, 6.01; N, 10.43. Found C, 71.82; H, 5.98; N, 10.35. $^1$H NMR ($CDCl_3$, 500 MHz, $\delta_H$, ppm) 3.9 (t, 4H, –CH), 6.8 (t, 2H, Ar), 6.9 (d, 2H, Ar), 7.2 (d, 2H, Ar), 7.3 (t, 2H, Ar), 8.3 (s, 2H, =CH), 13.2 (s, 2H, OH). *m/z*, ESI-MS: $[M + H]^+$, 267.11 (*calcd* 267.11). Liquid state IR ($CHCl_3$, $cm^{-1}$) $\nu(C=N)_{stretch}$ 1620. UV-vis spectrum ($CHCl_3$) [$\lambda$, nm ($\varepsilon$, $M^{-1}cm^{-1}$)]: 257 (27 000), 319 (10 500).

**2.2.5.6 2,2`-[1,4-Phenylenebis{(E)-nitrilomethylidyne}]bisphenol ($H_2$SPA).** A methanolic solution of 2-hydroxybenzaldehyde (0.226 g, 1.84 mmol) was added drop wise to a solution of *p*-phenylenediamine (0.100 g, 0.92 mmol) in methanol and the resulting solution was stirred for 4–6 hours to complete the reaction. It afforded a shiny yellow compound which was washed with methanol, hexane and diethyl ether and dried under vacuum. Yield 0.240 g (82%). Anal. *calcd* for $C_{14}H_{12}N_2O_2$: C, 75.93; H, 5.10; N, 8.86. Found C, 75.24; H, 5.13; N, 8.75. $^1$H NMR ($CDCl_3$, 500 MHz, $d_H$, ppm) 6.9 (t, 2H, Ar), 7.0 (d, 2H, Ar), B7.4 (s, 4H, Ar), 7.4 (t, 2H, Ar), 8.7 (s, 2H, =CH), 13.2 (s, 2H, OH). *m/z*, ESI-MS: $[M + H]^+$, 315.11 (*calcd* 315.11). Liquid state IR ($CHCl_3$, $cm^{-1}$) $\nu(C=N)_{stretch}$ 1606. UV-vis spectrum ($CHCl_3$) [$\lambda$, nm ($\varepsilon$, $M^{-1}cm^{-1}$)]: 274 (16 150), 370 (25 000).

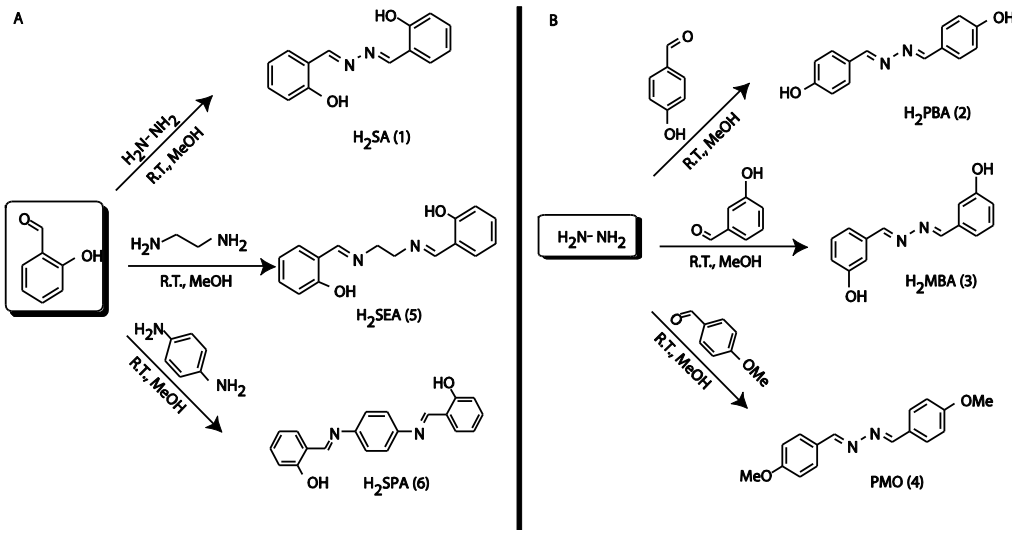


**Scheme 2.2** Synthetic routes adopted for the synthesis of compounds (A) **$H_2$SA**, **$H_2$SEA**, **$H_2$SPA** and (B) **$H_2$PBA**, **$H_2$MBA** and **PMO.**

## 2.3 RESULTS AND DISCUSSION

In order to monitor the role of L-tartaric acid based flexible chiral cores in gelation, as well as their contribution towards the gel properties,[4] in this chapter, we synthesized the smallest possible symmetrical aromatic low molecular weight ligand **$H_2$SA** (Scheme 2.1 and 2.2). The new ligand molecule contains two N, O donor metal chelation sites, and it is expected to achieve planar structure upon chelation which provides a platform for growth of building blocks/aggregation *via* π–π two regioisomers $H_2$PBA,[7] $H_2$MBA,[8] as well as other model compounds $H_2$SPA,[6] PMO,[10] $H_2$SEA,[9] were synthesized in good yield (80-90 %) with slight modification in literature procedures. The characterization data was found to be in full agreement with their proposed formulations (Scheme 2.2 and section 2.2). Ligand **$H_2$SA** (~$4x10^{-2}$ M) was dissolved in $CHCl_3$ followed by addition of methanolic solution of LiOH (~$8x10^{-2}$ M) turned into an opaque green-blue fluorescent gel (1%, w/v) instantly at ambient room temperature (Figure 2.1-2.3). The gelation was confirmed by conventional inverted vial test (Figure 2.1-2.3).

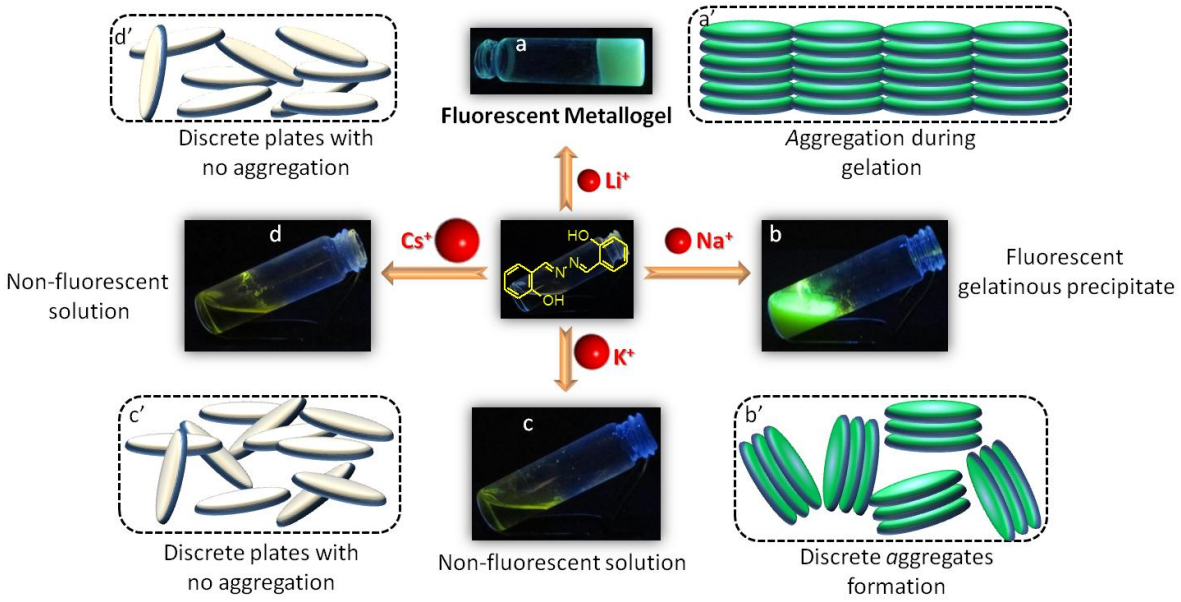


**Figure 2.1** Responses of **$H_2$SA** upon addition of two equivalents of (a) LiOH, fluorescent gel; (b) NaOH, fluorescent sol; (c) KOH, non-fluorescent sol and (d) CsOH, non-fluorescent sol. The corresponding models (a' to d') represent the possible molecular arrangement in respective gel or solution.

Further, optimization of gelation with **$H_2$SA** and methanolic LiOH in other common solvents leads to only suspension or solution rather than metallogel formation under similar conditions (Table 2.1). The other alkali bases like NaOH, KOH and CsOH also failed to produce metallogel under aforesaid similar conditions, which indicates the selectivity of ionic radius of $Li^+$ ion towards gelation (Table 2.2 and Fig. 2.3).[4,5] In addition, the role of higher solvation ability of $Li^+$ compared to other alkali metal ions towards gelation cannot be ruled out. To ensure about the role of alkali metal ion in gelation, we performed the gelation test with strong bases like tetrabutylammonium hydroxide (TBAOH) and triethyl amine ($Et_3N$), in turn, obtained a clear non-fluorescent solution which proves the importance of alkali base (Fig. 2.3). Interestingly, regioisomer **$H_2$PBA** could not pass the gelation test upon addition of LiOH and forms notable orange-yellow fluorescent solution under similar gelation conditions to **$H_2$SA**, indicating the importance of the position of –OH group in gel

formation. Further, position isomer **$H_2$MBA**, supporting ligand **PMO** and structurally flexible ligand **$H_2$SEA** afforded non fluorescent solution while the stiff **$H_2$SPA** imparts the fluorescent suspension at the gelation conditions to **1**. The gelation ability of compounds **$H_2$SA**, **$H_2$PBA**, **$H_2$MBA**, **PMO**, **$H_2$SEA** and **$H_2$SPA** in other solvents with methanolic LiOH has been summarized in table 2.1 and figure 2.4.

The above anomalous facts directly associated with the position of –OH group and type of central core (spacer); attracted our attention towards ligands being probable good candidates for the study of optical as well as aggregation properties. The freshly prepared gel demonstrated the stimuli response towards mechanical (shaking) or ultrasound (30 kHz) in a gel-sol reversible manner as well as the notable reswelling property as demonstrated in figure 2.2.

**Table 2.1** Gelation tests with respect to isomers, LiOH and solvents*

| Solvent | $H_2$SA+ LiOH | $H_2$PBA +LiOH | $H_2$MBA +LiOH | PMO +LiOH | $H_2$SEA +LiOH | $H_2$SPA +LiOH |
|---|---|---|---|---|---|---|
| **Water** | S | SP | SP | SP | SP | SP |
| **Acetonitrile** | S | S | S | S | S | S |
| **Methanol** | S | S | S | S | S | S |
| **Ethanol** | S | S | S | S | S | S |
| **DMF** | S | S | S | S | S | S |
| **DMSO** | S | S | S | S | S | S |
| **Acetone** | S | S | S | S | S | S |
| **Chloroform** | **G** | SP | S | S | S | SP |
| **DCM** | S | SP | S | S | S | SP |
| **THF** | S | S | S | S | S | S |

*Where, S= solution, G= gel, GP= Gelatinous precipitate, SP= Sparingly soluble

**Table 2.2** Gel or sol formation of **$H_2$SA** with different alkali bases*

| Solvent | $H_2$SA+LiOH | $H_2$SA+NaOH | $H_2$SA+KOH | $H_2$SA+CsOH |
|---|---|---|---|---|
| $CHCl_3$ | **G** | GP | S | S |

*Where, S= solution, G= gel, GP= Gelatinous precipitate

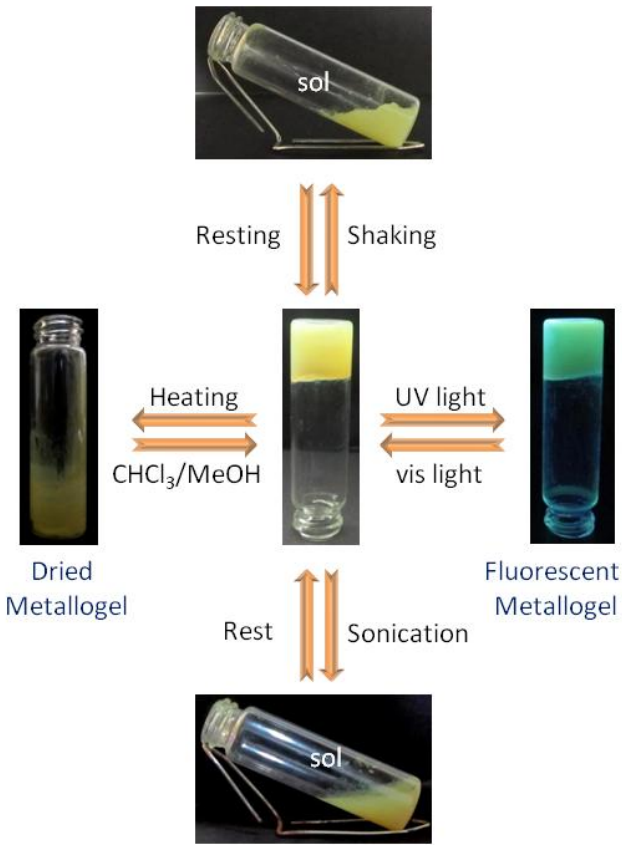


**Figure 2.2** Responses shown by gel under UV light irradiation, sonication, shaking, resting and heat. Note that heating of gel simply produces xerogel.

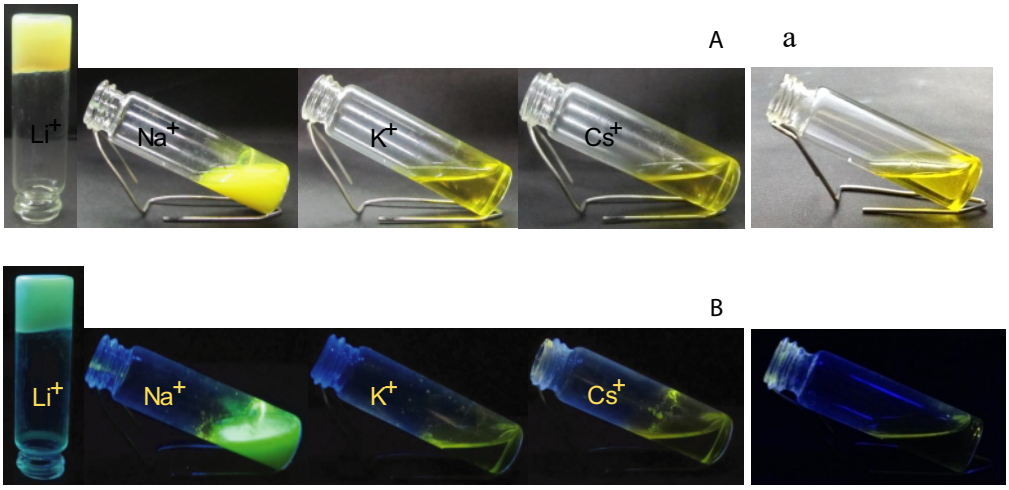


**Figure 2.3 (A)** Upper figure represents the gelation property of ligand **$H_2SA$** with $Li^+$, $Na^+$, $K^+$, $Cs^+$ and (a) TBAOH under necked eye and **(B)** Lower figure represents similar metallogel and sols under UV light (365 nm).

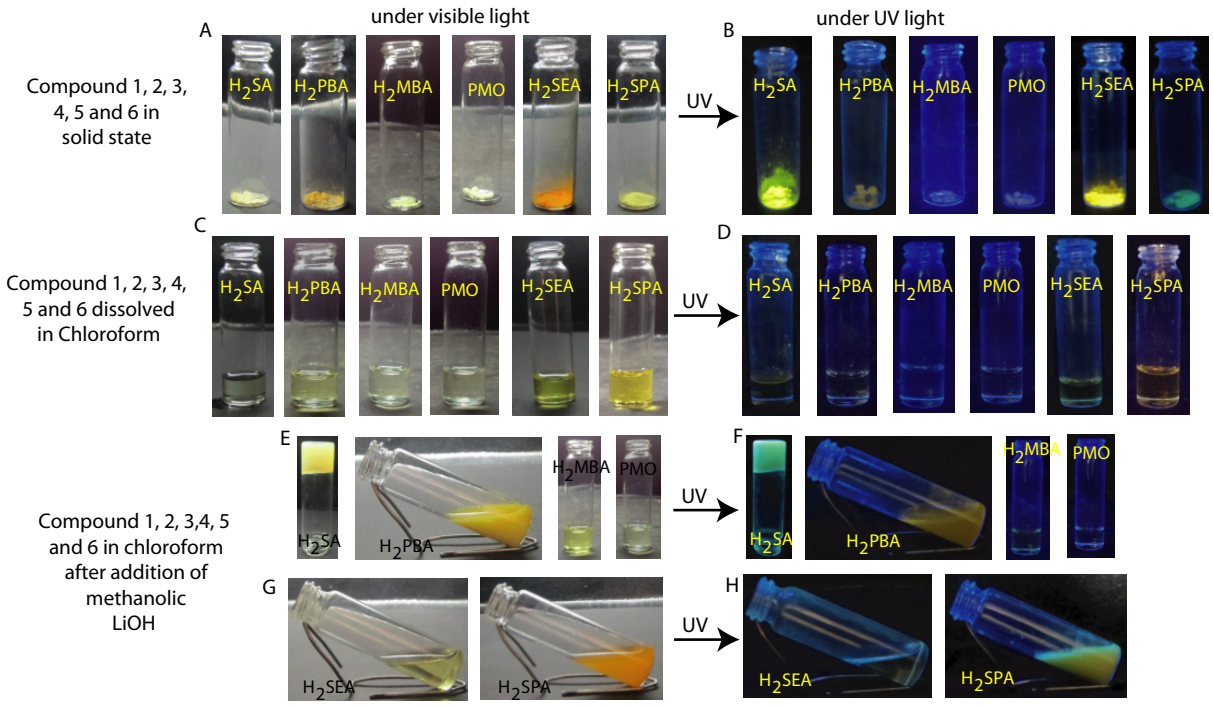


**Figure 2.4** A complete summary of **$H_2$SA**, **$H_2$PBA**, **$H_2$MBA**, **PMO**, **$H_2$SEA** and **$H_2$SPA** in solid state **(A)** under naked eye and **(B)** under UV light. Solid dissolved in $CHCl_3$ **(C)** under naked eye and **(D)** under UV light. Changes after addition of methanolic LiOH in all above mentioned nonfluorescent solutions under **(E & G)** visible light and **(F & H)** under UV light. (**$H_2$SA**, **PMO**, **$H_2$SEA** and **$H_2$SPA** were completely soluble in chloroform but **$H_2$PBA** and **$H_2$MBA** were soluble in chloroform/DMSO (4:1) and chloroform/Methanol (4:1) solvent mixture, respectively.)

## 2.4 MORPHOLOGICAL CHARACTERIZATION

The morphology of vacuum dried metallogel and the effect of other alkali metal ions obstructing gelation were monitored by SEM (Fig. 2.5 and 2.6). The xerogel (**$H_2$SA**/$Li^+$) shows a long-range fibrous network with an average diameter in the range of 100 to 200 nm, while a turbid solution of **$H_2$SA**/$Na^+$ reveals broken fibrous aggregates. Further, the clear solution of **$H_2$SA**/$K^+$ demonstrates the crystals along with random aggregates, while the combination of **$H_2$SA**/$Cs^+$ demonstrates single crystal growth. The morphological tuning from long range fibers to crystals with a sequential increment in the size of alkali metal ions clearly indicates that the gelation is strongly dependent on the size of the alkali metal ion

[4,5] and this type of morphological variation has not been reported, particularly with ultra-LMWG systems.

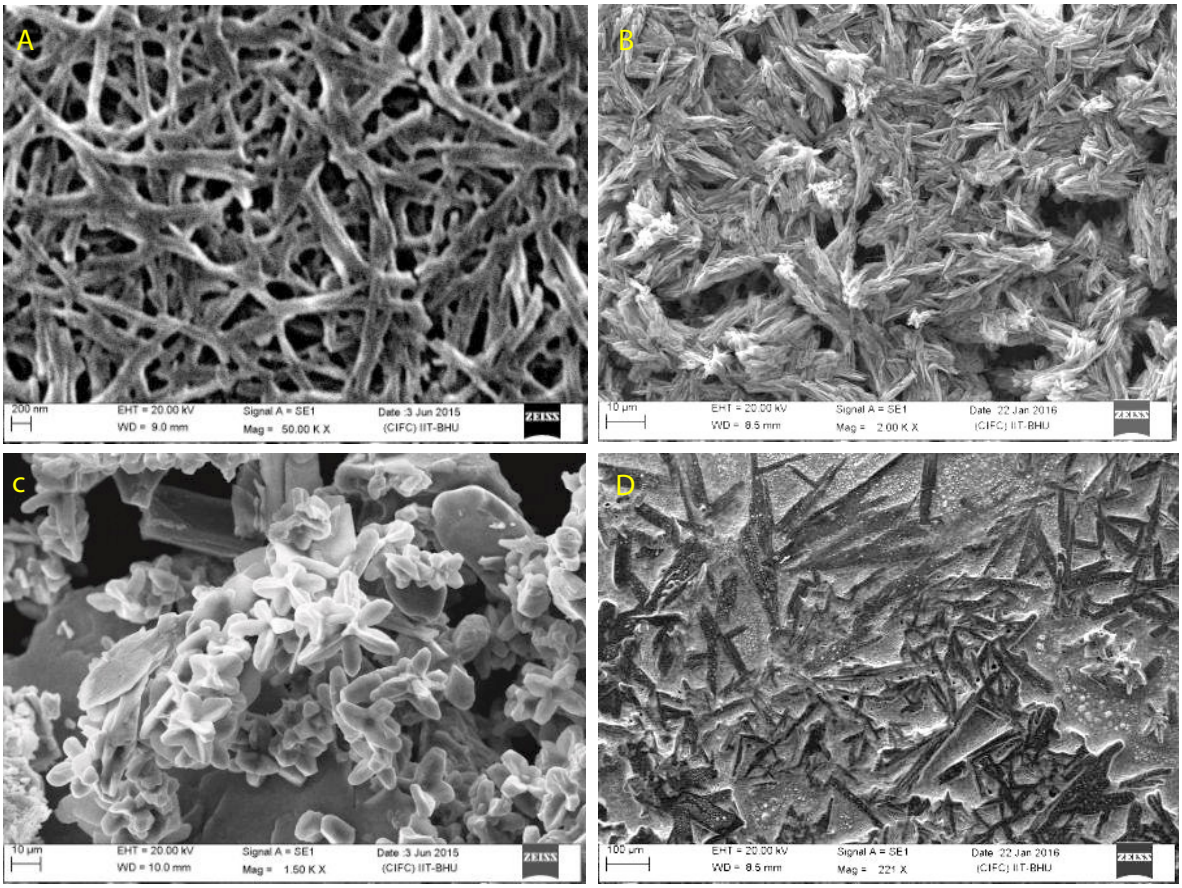


**Figure 2.5** SEM images of xerogel and dried solutions of (A) **$H_2$SA**/$Li^+$, (B) **$H_2$SA**/$Na^+$, (C) **$H_2$SA**/$K^+$ and (D) **$H_2$SA**/$Cs^+$ showing the fiber, broken fiber, crystalline morphology and crystals, respectively.

## 2.5 PXRD ANALYSIS

In order to support distinct morphological features, a powder X-ray diffraction pattern was analyzed between a $2\theta$ range of 10°–40° over various combinations of xerogel/dried sols and it was found that **$H_2$SA** loses its crystalline property and trans-forms into an amorphous material upon gelation (**$H_2$SA**/$Li^+$; xerogel) as is evident from the broadening of the peaks (Fig. 2.7).The crystallization of $Li^+$ as LiOH in an insignificant fraction during drying cannot

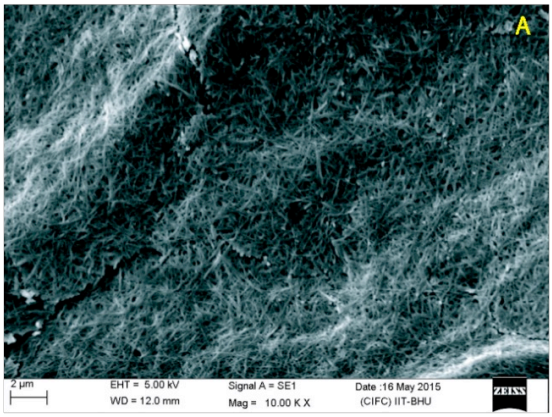
A
2 µm
EHT = 5.00 kV
WD = 12.0 mm
Signal A = SE1
Mag = 10.00 K X
Date :16 May 2015
(CIFC) IIT-BHU
ZEISS

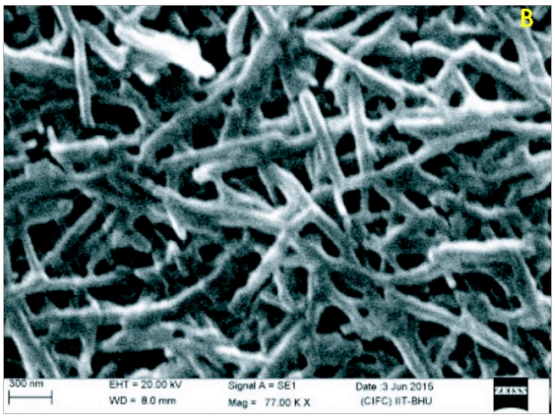
B
300 nm
EHT = 20.00 kV
WD = 8.0 mm
Signal A = SE1
Mag = 77.00 K X
Date :3 Jun 2015
(CIFC) IIT-BHU
ZEISS

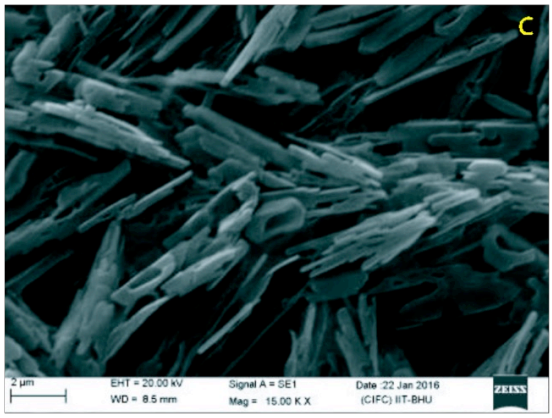
C
2 µm
EHT = 20.00 kV
WD = 8.5 mm
Signal A = SE1
Mag = 15.00 K X
Date :22 Jan 2016
(CIFC) IIT-BHU
ZEISS

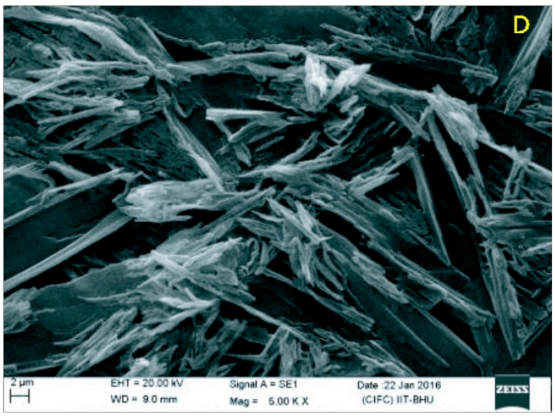
D
2 µm
EHT = 20.00 kV
WD = 9.0 mm
Signal A = SE1
Mag = 5.00 K X
Date :22 Jan 2016
(CIFC) IIT-BHU
ZEISS

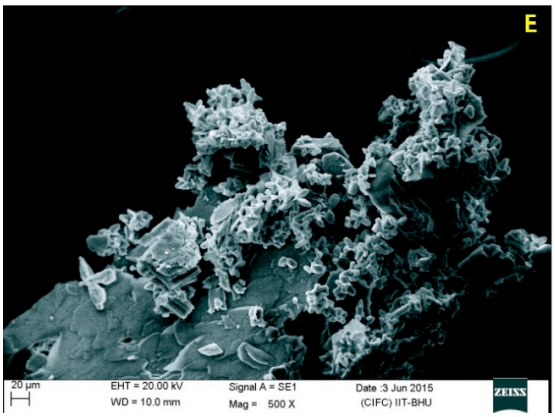
E
20 µm
EHT = 20.00 kV
WD = 10.0 mm
Signal A = SE1
Mag = 500 X
Date :3 Jun 2015
(CIFC) IIT-BHU
ZEISS

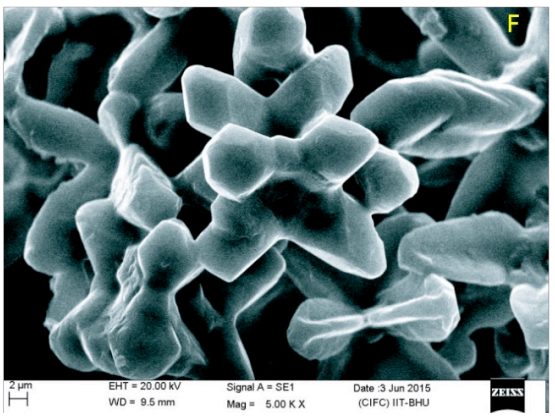
F
2 µm
EHT = 20.00 kV
WD = 9.5 mm
Signal A = SE1
Mag = 5.00 K X
Date :3 Jun 2015
(CIFC) IIT-BHU
ZEISS

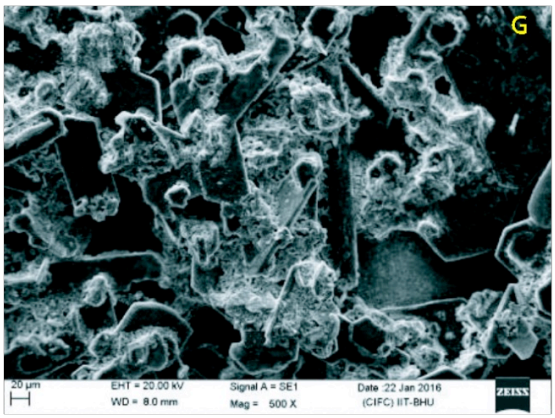
G
20 µm
EHT = 20.00 kV
WD = 8.0 mm
Signal A = SE1
Mag = 500 X
Date :22 Jan 2016
(CIFC) IIT-BHU
ZEISS

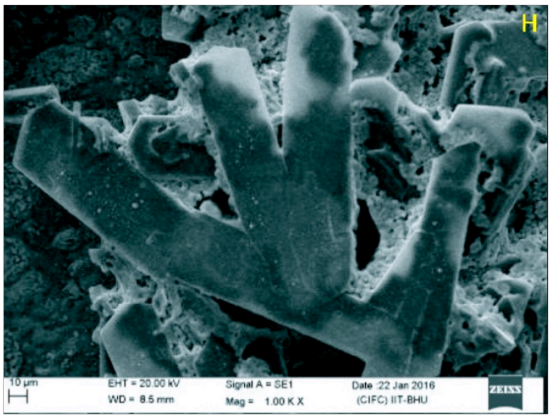
H
10 µm
EHT = 20.00 kV
WD = 8.5 mm
Signal A = SE1
Mag = 1.00 K X
Date :22 Jan 2016
(CIFC) IIT-BHU
ZEISS

**Figure 2.6** SEM images of **$H_2SA$**/$Li^+$ dried gel showing (**A and B**) long range fibrous morphology, dried sol of **$H_2SA$**/$Na^+$ showing (**C and D**) crystalline fibrous nature, dried sol of **$H_2SA$**/$K^+$ produced (**E and F**) crystals (morphology similar to flower) and dried sol of **$H_2SA$**/$Cs^+$ produced (**G and H**) normal rod shaped crystals.

be ruled out (Fig. 2.7). Further, appearance of sharp peaks in the case of **$H_2SA$**/$Na^+$ and **$H_2SA$**/$K^+$ signifies the crystalline nature and is comparable with peak patterns of **$H_2SA$**. The observation may be correlated with the presence of very weak electrostatic interactions between N, O donor and $Na^+$ or $K^+$ compared to $Li^+$ which indicates crystallization of **$H_2SA$** without an alkali metal ion. The pattern has no significant change in NaOH to KOH and CsOH which may be due to reversible binding of the alkali metal ion to the ligand **$H_2SA$**. Further, the assumption was proved right by determination of the structural and crystallographic parameters of the crystal obtained from the solution of **$H_2SA$**/CsOH which are in full agreement with the parameters reported for **$H_2SA$**, hence signifying the crystallization of **$H_2SA$** without an alkali metal ion.[14] Furthermore, to verify the crystallization of **$H_2SA$** without $Cs^+$, we performed PXRD on bulk crystals of **$H_2SA$**/$Cs^+$ which matches nicely with the simulated PXRD pattern of **$H_2SA$** (Fig. 2.7).[6,15] In addition, $^1$H NMR of crystals dissolved in $CDCl_3$ confirms the presence of phenolic protons. Further, the p$K_a$ of phenolic protons could not be estimated due to poor solubility in water, even in the presence of a DMF–water mixture. However, the presence of minor impurities like hydroxides and carbonates of respective alkali metal cations cannot be ruled out (Fig. 2.7). Among the prominent peaks in the PXRD pattern of the dried metallogel, the presence of four periodic diffraction peaks at $2\theta$ = 11.3, 22.5, 33.9 and 45.8 were analyzed and the corresponding *d*-values were found to be 7.8, 3.9, 2.6 and 1.9 nm, respectively, which followed a ratio of $d : d/2 : d/3 : d/4$ (Fig. 2.8). The periodic pattern of interspacing suggests

a layered organization within the aggregate of the metallogel. The interlayer distance was found to be 7.8 nm.[16]

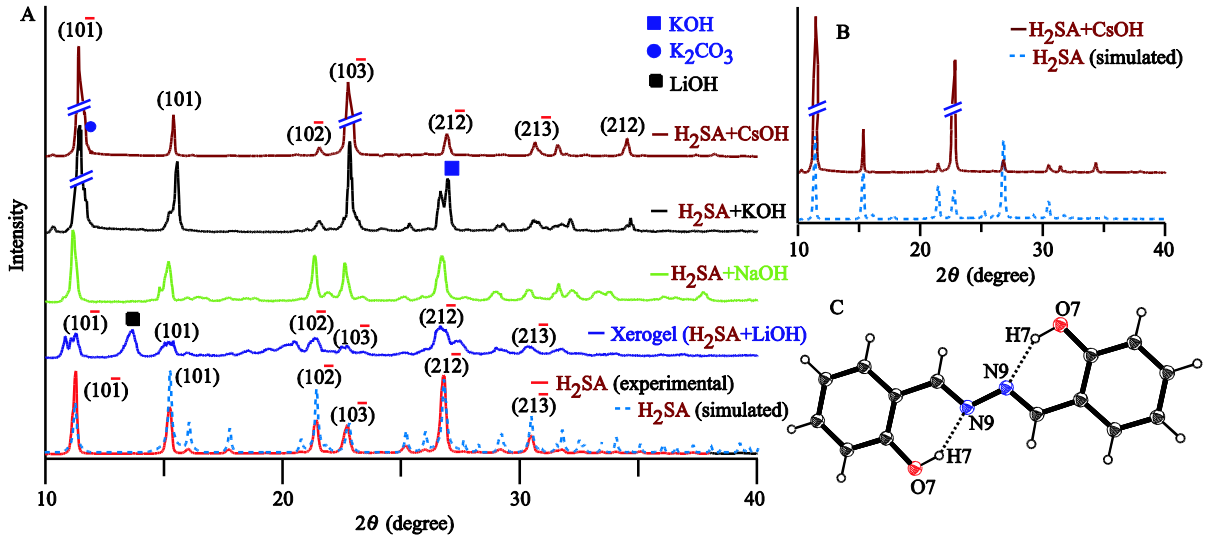


**Figure 2.7** Powder X-ray Diffraction pattern of (A) **$H_2$SA** (black line, experimental; blue dotted line, simulated), xerogel (orange line), gelator **$H_2$SA**/NaOH (red line), **$H_2$SA**/KOH (blue line) and **$H_2$SA**/CsOH (green line), respectively, (B) Comparison between and **$H_2$SA** (simulated) and crystals obtained from **$H_2$SA**/CsOH solution and (C) ORTEP view of gelator **$H_2$SA** drawn using 35% ellipsoids probability and hydrogen bonding between –OH and N atom.

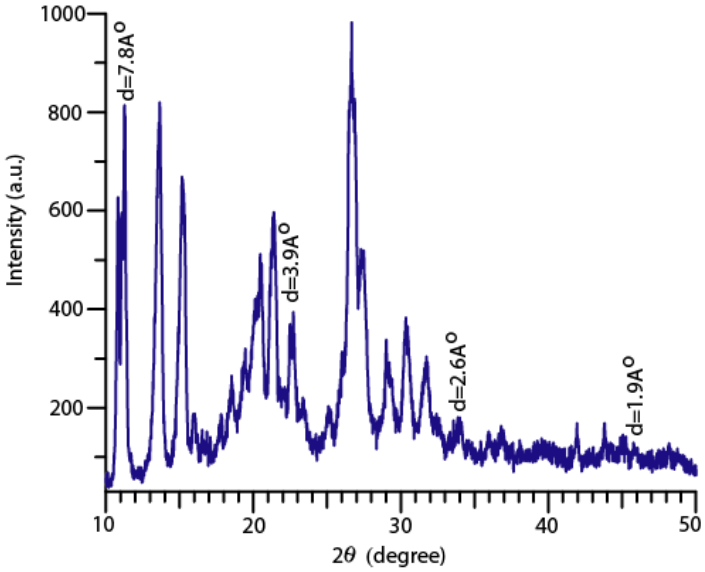


**Figure 2.8** The powder X-ray diffraction pattern of xerogel (**$H_2$SA**/$Li^+$).

## 2.6 UV-VIS STUDY

UV-vis experiments were performed to monitor the optical behavior of **$H_2SA$** with respect to the alkali metal ions *viz.*; $Li^+$, $Na^+$, $K^+$ and $Cs^+$ (Fig. 2.9 and 2.10). A light yellow colored solution of **$H_2SA$** ($1x10^{-5}$ M; $CHCl_3$) displayed two sharp bands at 363 nm ($\varepsilon$, 20700 $M^{-1}cm^{-1}$) and 295 nm ($\varepsilon$, 25800 $M^{-1}$ $cm^{-1}$) attributed to n–π* and π–π* transitions, respectively.[15,17] Further, upon aliquot addition of LiOH ($1x10^{-3}$ M, MeOH) to a solution of **$H_2SA$**, a concomitant decrease of the 363 nm band and appearance of a new band at 414 nm along with a broad hump at 390 through an isosbestic point at 386 nm was observed. This suggests deprotonation of the phenolic proton as well as chelation of $Li^+$ with **$H_2SA$** in an N, O fashion. In addition, the band at 295 nm hypochromically blue shifted to 286 nm ($\Delta\lambda$ = 9 nm) due to the introduction of the π–π stacking interaction. On the other hand, addition of NaOH to **$H_2SA$** under aforementioned similar conditions also showed the simultaneous transformation of the 363 nm band into a 401 nm band through an isosbestic point at 377 nm, while the band at 295 nm showed only a hypochromic shift. Similarly, **$H_2SA$**/$K^+$ and **$H_2SA$**/$Cs^+$ demonstrated the conversion of a 363 nm band into 414 nm and 417 nm bands, respectively, through an isosbestic point at ~383 nm. Remarkably, the band at 295 nm did not offer any significant shift, except the decrease in absorbance at 295 nm only upon addition of $K^+$ or $Cs^+$ ions which were due to a lack of π–π stacking in solution (*vide infra*). The difference in spectral behavior of **$H_2SA$** with $Li^+$ relative to $Na^+$, $K^+$ and $Cs^+$ ions is due to the difference in size of alkali metal ions or the interaction/suitability to fit in the N, O binding site. In other words, $Li^+$ only showed the ability to make effective interactions with **$H_2SA$** and helped in the formation of a gel, while $Na^+$, $K^+$ and $Cs^+$ resulted in solutions which were well supported by their morphology and PXRD pattern. Further, bigger size non-alkali

strong base TBAOH also showed spectral changes similar to $Cs^+$ while weak bases like $NEt_3$ or $NH_3$ failed to initiate changes; this suggests the vital role of strength of base as well as size of alkali metal ion in gelation (Fig. 2.11). Upon aliquot addition of LiOH under aforesaid gelation conditions, regioisomer **$H_2$PBA** as well as other supporting ligands **$H_2$SEA** and **$H_2$SPA** exhibited an almost similar kind of concomitant conversion of their one band 323/319/370 nm into another new band 380/337/397 nm through an isosbestic point at 347/324/387 nm, respectively (Fig. 2.12). Regioisomer **$H_2$MBA** and auxiliary ligand **PMO** produce almost unchanged spectra with their $\lambda_{max}$ at 303 nm and 330 nm, respectively (Fig. 2.12). Thus, it is expected that LiOH first deprotonates the –OH and then $Li^+$ interacts with O or N, O donor atoms *via* electrostatic interaction.

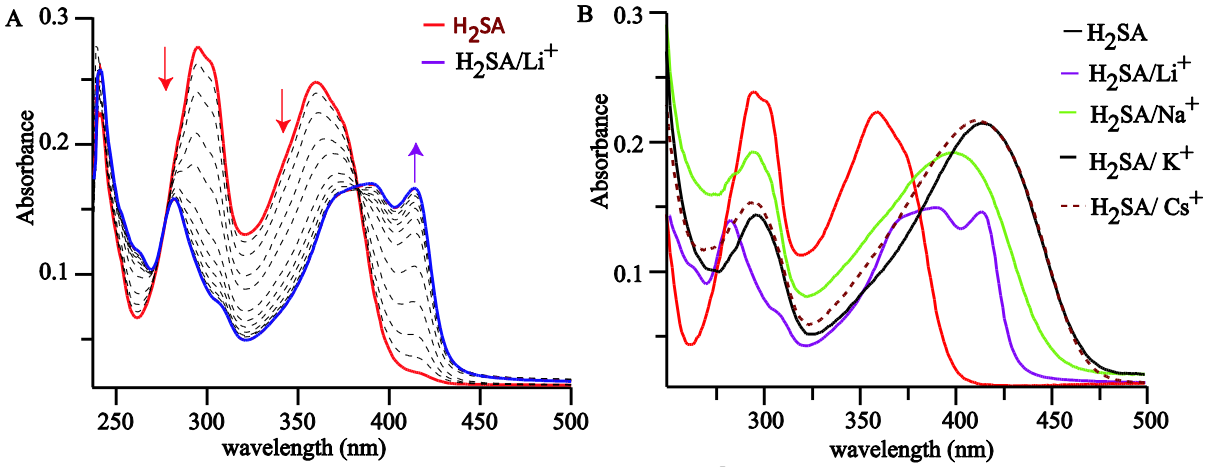


**Figure 2.9** (**A**) UV-vis titration spectra of **$H_2$SA** ($1x10^{-5}$ M, $CHCl_3$, red line) *vs*. LiOH ($1x10^{-3}$ M, $CH_3OH$, black dotted and blue lines) and (**B**) A comparative UV-vis spectrum of **$H_2$SA** ($1x10^{-5}$ M, $CHCl_3$, red line) *vs.* LiOH (blue line), NaOH (green line), KOH (black line) and CsOH (magenta line).

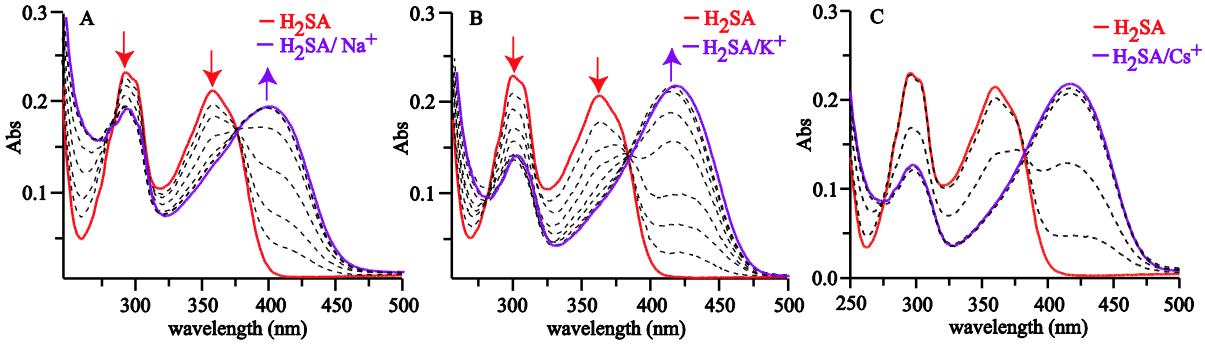


**Figure 2.10** UV-vis titration of **$H_2SA$** ($1x10^{-5}$M; $CHCl_3$) with (A) NaOH ($1x10^{-3}$M; $CH_3OH$) leads to hypochromic shift at 295 nm and red shift ($\Delta\lambda$=39 nm) of band at 363 nm to 402 nm, (B) KOH ($1x10^{-3}$M; $CH_3OH$) again produces hypochromic shift along with blue shift ($\Delta\lambda$=51 nm) to new band at 414 nm at the expense of 363 nm peak and (C) CsOH ($1x10^{-3}$M; $CH_3OH$) produces similar effect in which blue shift of 54 nm in band at 363 nm was observed.

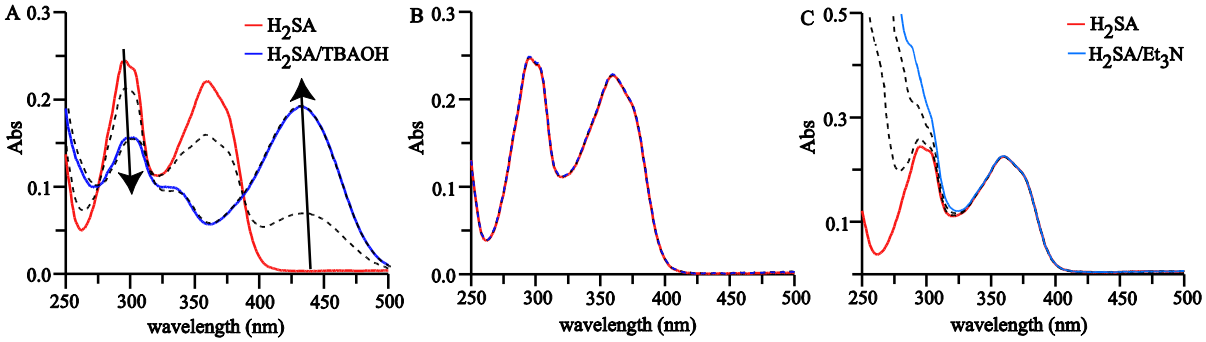


**Figure 2.11** (A) UV-vis spectrum of **$H_2SA$** ($1x10^{-5}$M; $\varepsilon$, 22800 $M^{-1}$ $cm^{-1}$; $CHCl_3$, red line) with TBAOH ($1x10^{-3}$M; $CH_3OH$, blue line) undergoes decrease in absorbance of band at 294 nm with slight red shift to 302 nm and peak at 363 nm converts in to new absorption band at 433 nm ($\Delta\lambda$= 70 nm) with a hump at around 334 nm, (B) and (C) treatment of $NH_3$ and $Et_3N$ to **$H_2SA$** do not produce any significant change.

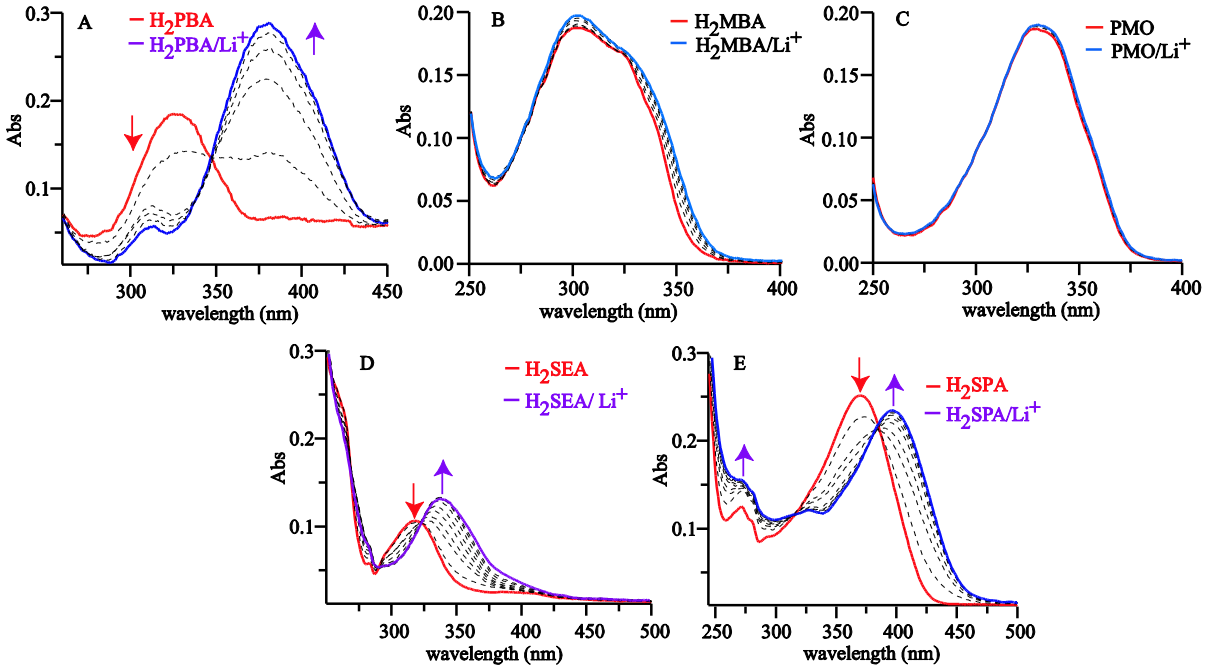


**Figure 2.12** (A) **$H_2$PBA** (1x10$^{-5}$ M; $\varepsilon$, 18 500 M$^{-1}$cm$^{-1}$; $CHCl_3$/DMSO, 4:1) upon addition of LiOH (1x10$^{-3}$M; $CH_3OH$) demonstrates the red shift to 380 nm ($\Delta\lambda$=57 nm) with an isosbestic point at 348 nm, (B) Structural isomer **$H_2$MBA** appeared at 303 nm (1x10$^{-5}$ M; $\varepsilon$, 18 300 M$^{-1}$cm$^{-1}$; $CHCl_3$/MeOH, 4:1), (C) compound **PMO** (1x10$^{-5}$ M; $\varepsilon$, 19 500 M$^{-1}$cm$^{-1}$, $CHCl_3$) at 330 nm do not show any significant change after addition of LiOH (1x10$^{-3}$M; $CH_3OH$), (D) **$H_2$SEA** (1x10$^{-5}$M; $\varepsilon$, 10500 M$^{-1}$cm$^{-1}$; $CHCl_3$) appears at 319 nm which upon LiOH (1x10$^{-3}$M; $CH_3OH$) addition shifted to 337 nm ($\varepsilon$, 13300 M$^{-1}$cm$^{-1}$; $CHCl_3$) through an isosbestic point and (E) **$H_2$SPA** showed peak at 370 nm (1x10$^{-5}$M; $\varepsilon$, 25 000 M$^{-1}$cm$^{-1}$; $CHCl_3$) in presence of LiOH (1x10$^{-3}$ M, $CH_3OH$) red shifted to 397 nm with an isosbestic point.

## 2.7 FLUORESCENCE STUDY

The fluorescence experiments were executed in order to scrutinize the selectivity of ligand **$H_2$SA** and $Li^+$ towards gelation over other alkali metal ions or other rationally structurally close ligands - **$H_2$PBA**, **$H_2$MBA**, **PMO**, **$H_2$SEA** and **$H_2$SPA**. **$H_2$SA** ($\lambda_{ex}$ = 363 nm, 1x10$^{-3}$ M, $CHCl_3$) displayed a very weak emission band at 534 nm (Stokes shift = ~8800 cm$^{-1}$) but subsequent addition of methanolic LiOH leads to the appearance of the blue shifted ($\Delta\lambda$ = 77 nm) band at 457 nm with a notable large (~1000 fold) increment in emission intensity (Fig. 2.13). The almost non-emissive characteristic of **$H_2$SA** and the highly emissive nature of

**$H_2SA$**/$Li^+$ may be due to two well-known phenomena *viz*. excited-state intramolecular proton-transfer (ESIPT) and chelation enhanced fluorescence (CHEF), respectively.[18,19] Among the reported examples, nearly all ESIPT-based molecules exhibit emission in the visible region (400–650 nm) with large Stokes shift (8500–10 500 $cm^{-1}$) and deprotonation of a phenolic proton followed by metal binding inhibits the ESIPT permanently.[20] Further, NaOH addition to **1** also leads to enhancement in intensity but with a lesser blue shift at 504 nm ($\Delta\lambda$= 30 nm, Stokes shift = 7700 $cm^{-1}$) indicating a weaker interaction than with $Li^+$ (*vide supra*, Fig. 2.14).

Moreover, upon addition of a bigger size alkali metal ion, $K^+$ or $Cs^+$, to **$H_2SA$**, the ensuing entity **$H_2SA$**/$K^+$ or **$H_2SA$**/$Cs^+$ exhibited blue shift at 504 nm ($\Delta\lambda$ = 30 nm) and 519 nm ($\Delta\lambda$ = 15 nm), respectively, but with a much weaker emission intensity than **$H_2SA$**/$Li^+$ and **$H_2SA$**/$Na^+$, suggesting a weak interaction with **$H_2SA$** compared to $Li^+$ or $Na^+$ (Fig. 2.13 and 2.14). In extension, TBAOH could not produce any significant change in the emission spectra of **$H_2SA$** (Fig. 2.15). Thus, the successive decrease in blue shift and emission intensity with respect to increment in size of alkali metal ions exclusively supports the observation made in UV-vis and morphology.

To probe the CHEF phenomenon, we synthesized region-isomer **$H_2PBA$** by shifting the –OH group from the *ortho* to the *para* position with an objective of obstructing the chelation site. Surprisingly, the weak fluorescent solution of **$H_2PBA$** ($\lambda_{ex}$ = 323 nm, $\lambda_{em}$= 530 nm, $1x10^{-3}$ M, $CHCl_3$/DMSO, 4:1) turned into a highly emissive solution upon addition of LiOH ($1x10^{-1}$ M, $CH_3OH$) and exhibited a red shifted band at 565 nm ($\Delta\lambda$ = 35 nm) with a notably large

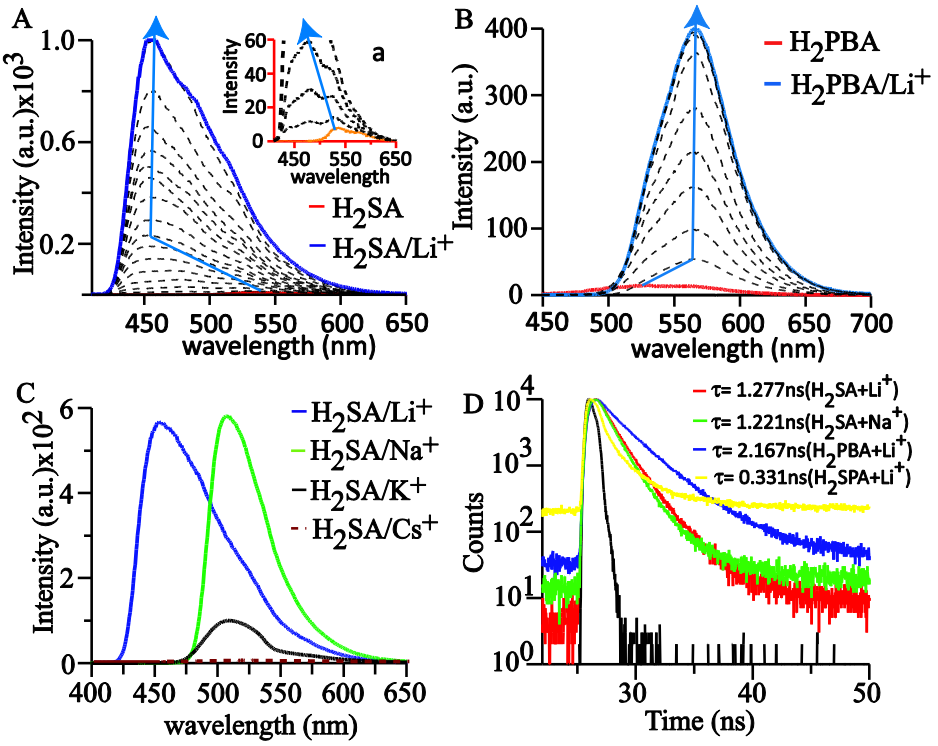


**Figure 2.13** (A) Fluorescence titration spectra of **$H_2$SA** ($\lambda_{ex}$ = 363 nm, 1x10$^{-3}$M, $CHCl_3$, red line) *vs*. LiOH (1x10$^{-1}$M, MeOH, black dotted and blue lines), inset of A shows the initial change; (B) fluorescence titration spectra of **$H_2$PBA** ($\lambda_{ex}$ = 323 nm, 1x10$^{-3}$M, $CHCl_3$) *vs*. LiOH (1x10$^{-1}$M, MeOH, black dotted line and blue lines) under similar conditions to A; (C) fluorescence spectra demonstrating the effect of size of the alkali metal ion over **$H_2$SA** and (D) a fluorescence lifetime plot ($\tau_{av}$) of **$H_2$SA**/Li$^+$, **$H_2$SA**/Na$^+$, **$H_2$PBA**/Li$^+$, **$H_2$SPA**/Li$^+$ shown in red, green, blue and yellow lines, respectively.

Stokes shift of 13 300 cm$^{-1}$, albeit, in the absence of a chelation site. At this stage, we assumed that the phenomenon of intramolecular charge transfer (ICT) occurs from the lone pair of N to para –O$^-$Li$^+$ in a synergic or push–pull manner which is supported by the aforementioned large Stokes shift (Fig. 2.19).[21] To further justify our assumption, we prepared meta positioned –OH regioisomer **$H_2$MBA** with an intention to inhibit ICT due to the absence of conjugation which obstructs the flow of charge from the imine N to –O$^-$Li$^+$ (Fig. 2.19). Moreover, our strategy worked well and **$H_2$MBA** remained non-fluorescent ($\lambda_{ex}$ = 303 nm, 1x10$^{-3}$ M, $CHCl_3$) upon addition of LiOH under similar conditions to **$H_2$PBA** (Fig. 2.16). In addition, the push–pull or synergic mechanism behind ICT is also attested by

the addition of LiOH to the solution of para –OMe containing **PMO** ($\lambda_{ex}$ = 330 nm, 1x10$^{-3}$ M, $CHCl_3$) which, in turn, exhibited lack of emission (Fig. 2.16).

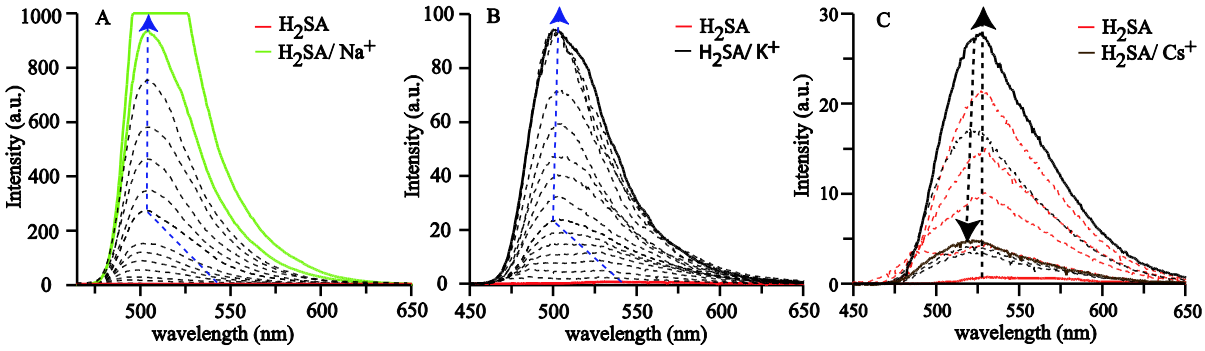


**Figure 2.14** Fluorescence titration between **$H_2SA$** ($\lambda_{ex}$= 363 nm, 1x10$^{-3}$ M, $CHCl_3$) and (A) NaOH (10$^{-1}$ M, MeOH), (B) KOH (10$^{-1}$ M, MeOH) and (C) CsOH (10$^{-1}$ M, MeOH) demonstrates the fluorescence intensity is inversely proportional to cation size.

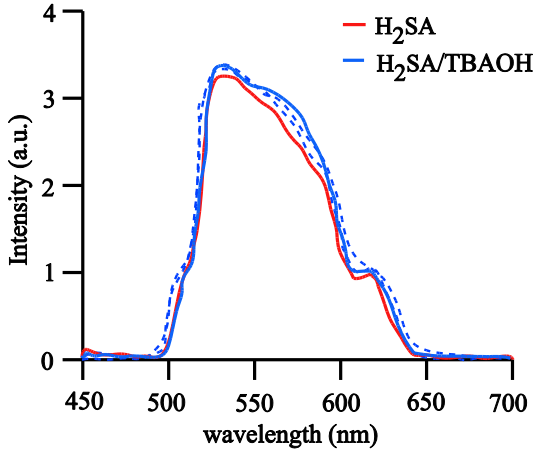


**Figure 2.15** TBAOH (10$^{-1}$M; MeOH) addition to **$H_2SA$** (10$^{-3}$ M; $CHCl_3$) remain unchanged fluorescence spectral properties.

In order to elucidate the $Li^+$ triggered ICT generation in **$H_2$PBA**, we performed titration between ICT based complex **$H_2$PBA**/$Li^+$ ($\lambda_{ex}$ = 323 nm, $1x10^{-3}$ M, $CHCl_3$/DMSO/$CH_3OH$) and [12]-crown-4 ether ($1x10^{-1}$ M, $CH_3OH$) (Fig. 2.17). Aliquot addition of [12]-crown-4 to the fluorescent solution of **$H_2$PBA**/$Li^+$ results in a decrease in

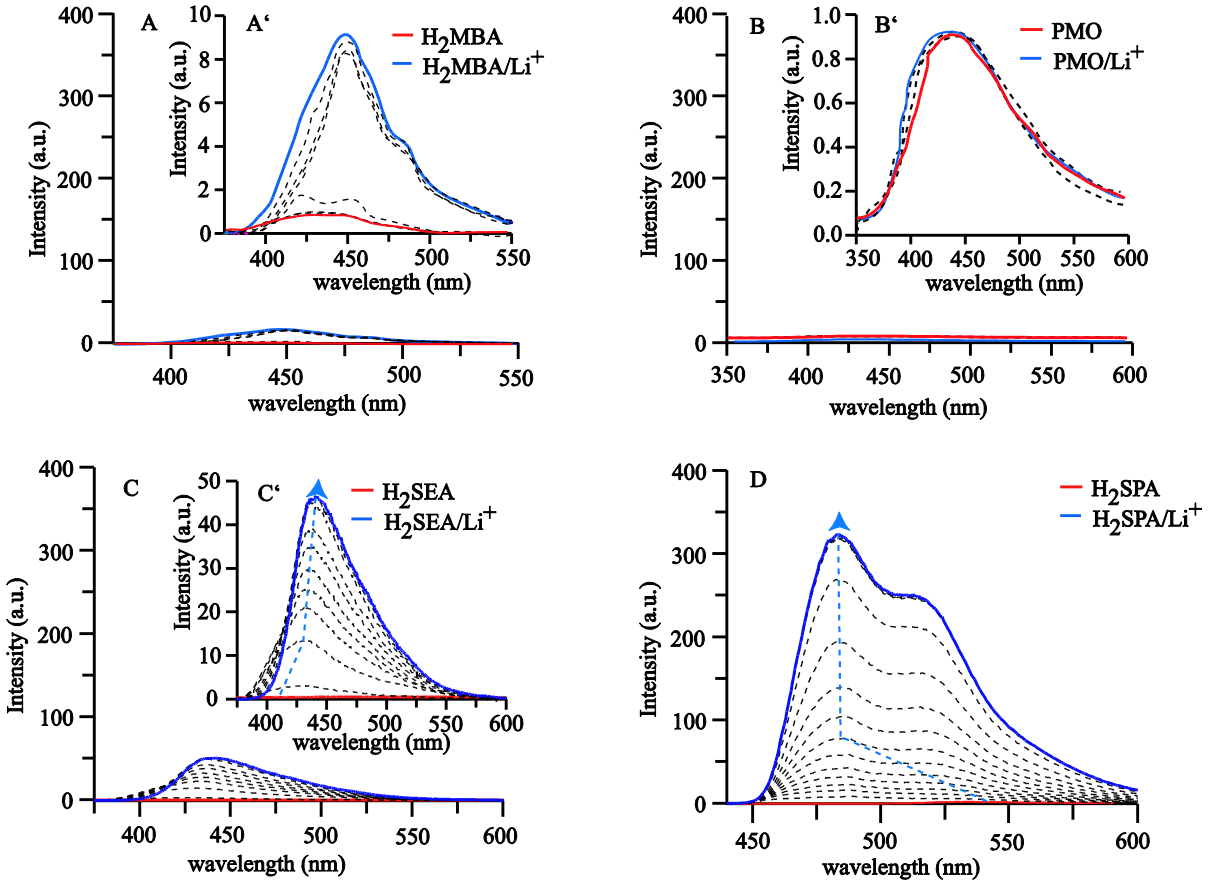


**Figure 2.16** Fluorescence spectrum of **(A)** and **(A')** **$H_2$MBA** (red line) after LiOH addition (blue line), similarly, **(B)** and **(B')** **PMO** ($\lambda_{ex}$ = 330nm, $1x10^{-3}$ M; $CHCl_3$) remains non fluorescent with LiOH. **(C)** and **(C')** non emissive **$H_2$SEA** ($\lambda_{ex}$ = 319 nm, $1x10^{-3}$ M; $CHCl_3$) displayed a peak at 410 nm (stokes shift= 85500 $cm^{-1}$) which upon gradual addition of LiOH ($1x10^{-1}$ M; MeOH) obtained a red shift with minor enhancement in fluorescent intensity at 436nm, **(D)** non emissive **$H_2$SPA** ($\lambda_{ex}$ = 370nm, $1x10^{-3}$ M; $CHCl_3$) at 435 nm (stokes shift= 85500$cm^{-1}$) displays hypsochromic blue shift ($\Delta\lambda$=45nm) upon addition of LiOH ($1x10^{-1}$M; MeOH).

intensity of the 565 nm band and the concomitant appearance of a band at 535 nm corresponding to ligand **$H_2$PBA** through an isosbestic point at 490 nm. Further, a plot of

equivalents of [12]-crown-4 added and emission intensity at 565 nm shows that two equivalents of [12]-crown-4 are required for complete trapping of $Li^+$ ions from the **$H_2$PBA**/$Li^+$ complex. Thus, generation of non-fluorescent **$H_2$PBA** from highly fluorescent solution of **$H_2$PBA**/$Li^+$ advocated the role of $Li^+$ in ICT generation.[15] The non-fluorescent nature of **$H_2$SEA** ($\lambda_{ex}$ = 319 nm, 1x$10^{-3}$ M, $CHCl_3$) remains unchanged upon addition of methanolic LiOH.[31]

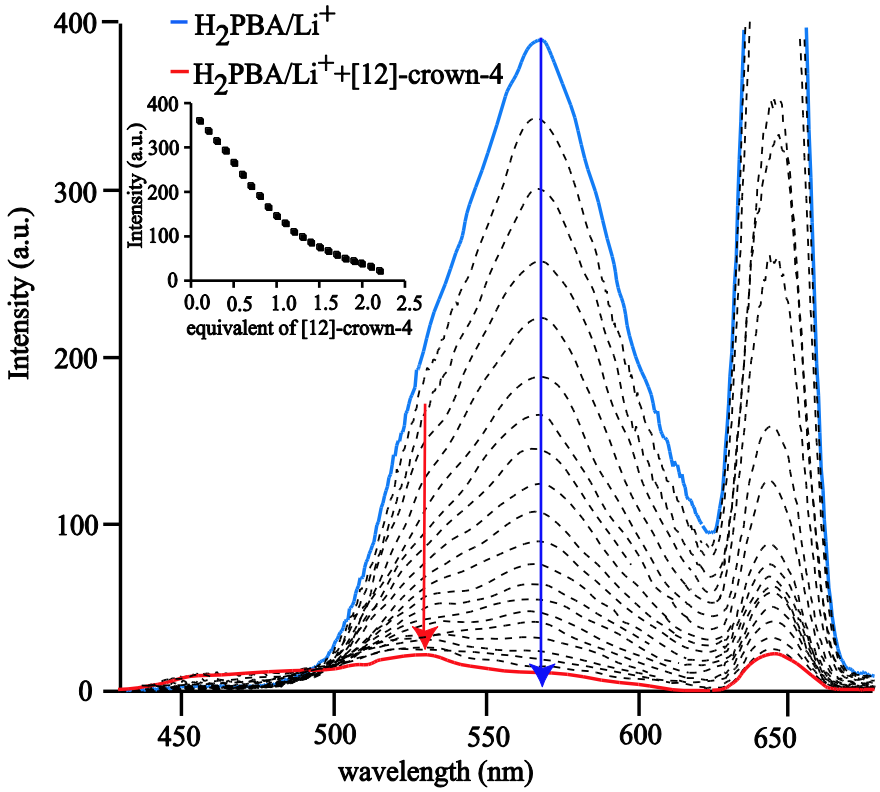


**Figure 2.17** A fluorescence titration of **$H_2$PBA**/$Li^+$ ($\lambda_{ex}$ = 323nm, $\lambda_{em}$ = 565nm, $10^{-3}$M, $CHCl_3$/MeOH) and [12]-crown-4 (1x$10^{-1}$M, $CH_3OH$). The inset plot shows fluorescence intensity (at 565 nm) against equivalents of crown ether ([12]-crown-4) added. The strong band at 646 nm is the twofold overtone wavelength for the excitation wavelength (323 nm).

The lack of fluorescence even after $Li^+$ chelation may be due to the flexible middle core, which restricts itself from achieving a rigid structure, followed by the enhancement in radiationless deactivation from its excited state.[22] Further, to ascertain the CHEF phenomenon and role of middle core in the appearance of fluorescence, we synthesized

structurally rigid conjugation enriched ligand **$H_2$SPA** and, as expected, it exhibited an emission band at 481 nm ($\lambda_{ex}$ = 370 nm, 1x$10^{-3}$ M, $CHCl_3$, Stokes shift = ~6200 $cm^{-1}$) upon addition of LiOH (Fig. 2.16). It is worth mentioning that **$H_2$SPA** forms a precipitate rather than a gel unlike **$H_2$SA**, although both are rationally close systems in terms of binding sites, rigidity and fluorescence behavior is possibly due to less planar structure.[23] Average lifetimes determined for **$H_2$SA**/$Li^+$, **$H_2$SA**/$Na^+$, **$H_2$PBA**/$Li^+$ and **$H_2$SPA**/$Li^+$ and found to be $\tau$ = 1.277, 1.221, 2.167 and 0.331 ns, respectively (Fig. 2.13 and section 2.2.4). The aforementioned different fluorescence can be attributed to a considerable decrease in the energy gap between the highest occupied molecular orbital (HOMO) and lowest unoccupied molecular orbital (LUMO), resulting in a red shift in emission spectra (Fig. 2.16).[24] Thus, the small change in the middle core and position of –OH affects the gelation and fluorescence properties.

To achieve better mechanistic insights into the gelation, a dilution experiment of freshly prepared metallogel was carried out within range of $10^{-2}$M to $10^{-4}$M. A 2.3 fold enhancement in fluorescence intensity, with a significant blue shift of 25 nm, was observed within the dilution range $10^{-2}$M to $10^{-3}$M, due to the presence of an aggregation caused quenching (ACQ) phenomenon. Further dilution ($10^{-3}$M–$10^{-4}$M) leads to complete quenching of intensity due to excessive dilution of the **$H_2$SA**/$Li^+$ species (Fig. 2.18). Further, variable temperature experiments were performed to demonstrate the reswelling nature of the metallogel (Fig. 2.18). Upon heating up to 70 $^oC$, a significant decrease (three fold) in the emission intensity was observed due to vaporization of the solvent from the gel network followed by xerogel formation. Further, upon *in situ* addition of a mixture of $CHCl_3$ and methanol (4:1) solvents to the xerogel, fluorescence intensity was recovered up to ~85% of

the freshly prepared gel which supports the observation made about the reswelling nature of the metallogel (Fig. 2.2 and Fig. 2.18).

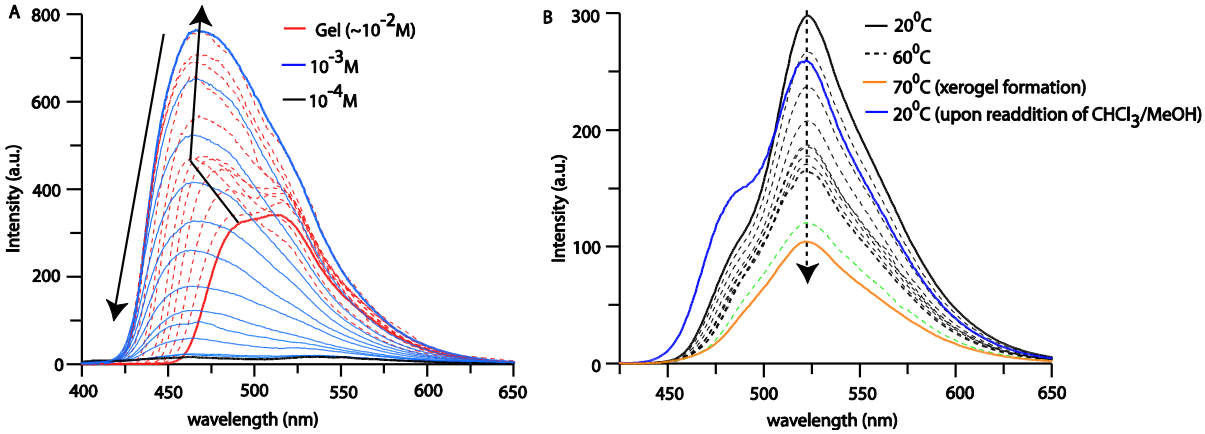


**Figure 2.18** (A) The effect of dilution (with $CHCl_3$) on fluorescence spectra of metallogel **$H_2$SA**/$Li^+$ ($\lambda_{ex}$ = 363 nm, ~$10^{-2}$ M; $CHCl_3$/$CH_3OH$, red line) which displayed two step spectral changes *i.e.*, $10^{-2}$ to $10^{-3}$ M fluorescence intensity enhancement followed by complete quenching from $10^{-3}$ to $10^{-4}$ M.

## 2.8 $^1$H NMR STUDY

To probe the weak interactions involved in the gelation process, we performed a $^1$H NMR titration experiment between **$H_2$SA** and LiOH under similar gelation conditions in $CDCl_3$/$CD_3OD$ (Fig. 2.20). The $^1$H NMR spectrum of **$H_2$SA** showed labile –OH protons appear at $\delta$ = 11.4 ppm, aldimine protons at 8.72 ppm and aromatic protons between 7.45 and 7.0 ppm. Upon aliquot addition of a $CD_3OD$ solution of LiOH to **$H_2$SA**, it was observed that the slightly higher degree of up field shifting ($\Delta\delta$ = 0.1 ppm) for aldimine protons (–N=CH), as well as the disappearance of –OH protons, signifies the chelation of $Li^+$ to '–CH=N' and the phenolate site. The broadening of peaks upon further addition of LiOH (2 equiv.) may be due to aggregation. The noticeable up field shift of other aromatic protons due to π–πinteractions during gelation cannot be ignored in the titration experiment. Thus, the conclusion drawn based on experimental results indicates that the chelation of $Li^+$, as well as π–π stacking factors, are mainly responsible for gel formation as illustrated in Fig. 2.2, 2.21

and 2.23. On the other hand, a detailed mechanism behind the appearance of fluorescence, as well as the possible molecular arrangement in solution of various other supporting ligands, is depicted in Fig. 2.19.

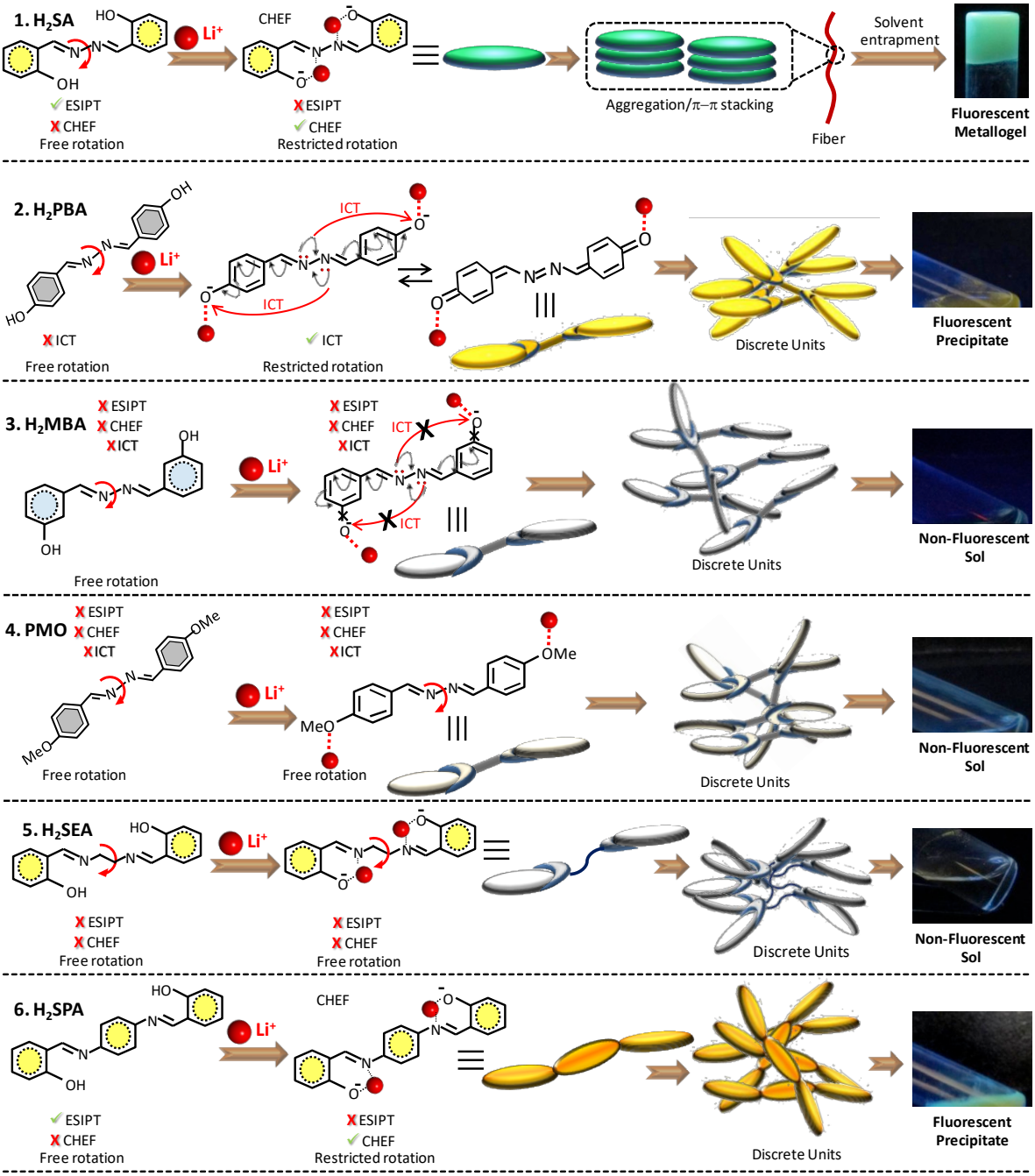


**Figure 2.19** Sketch and model diagrams represents mechanism- 1) N, O donor ligand **$H_2SA$** in protonated form active for ESIPT and $Li^+$ interaction trigger the blue green fluorescence followed by metallogel formation due to CHEF and aggregation, respectively. 2) Movement of –OH to para position in **$H_2PBA$** produced yellow fluorescent precipitate with $Li^+$ due to

ICT. 3) Reshuffling of –OH to meta in **$H_2$MBA** and treatment with LiOH shows non-fluorescent solution due to disturbance in conjugation proves the presence of ICT in **$H_2$PBA**. 4) Para –OMe containing **PMO** also supports the presence of ICT in **$H_2$PBA**/$Li^+$. 5) Ethylene moiety was introduced as a spacer to disturb ICT and the effect of CHEF due to high degree of free rotation. 6) Again, to prove ESIPT in neutral form and CHEF with $Li^+$ complexation, a benzene ring was introduced as a spacer, in turn, **$H_2$SPA**/$Li^+$ shows yellow fluorescent precipitate.

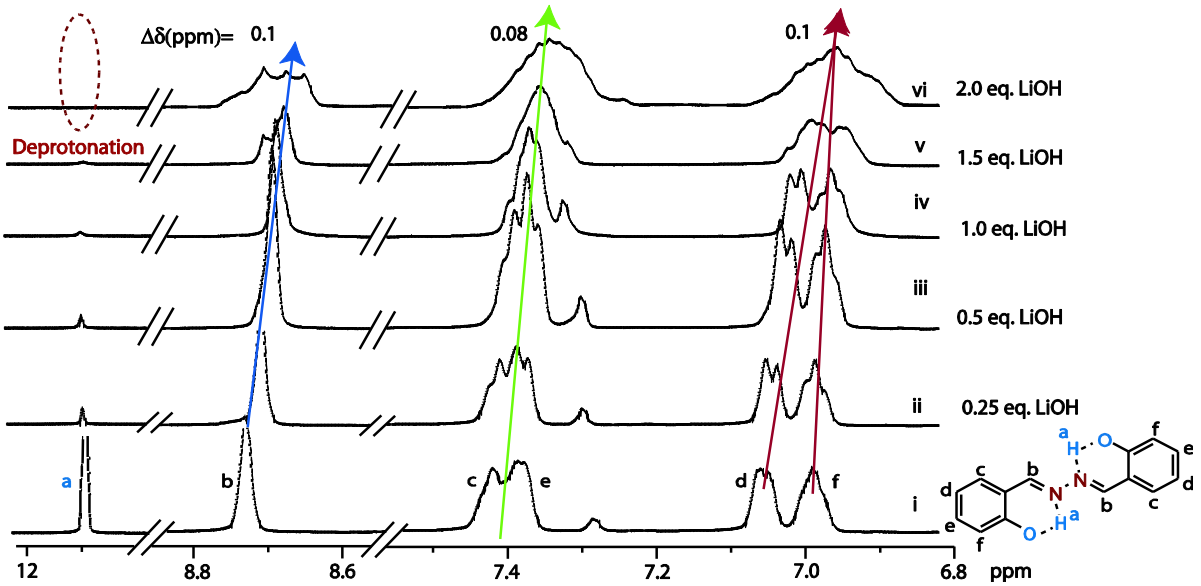


**Figure 2.20** $^1$H NMR titration spectrum of **$H_2$SA** ($CDCl_3$) with piecemeal addition of 4 equivalents of LiOH ($CD_3OD$). Chemical structure of **$H_2$SA** along with alphabetic assignment of protons and its corresponding peak shown in spectrum.

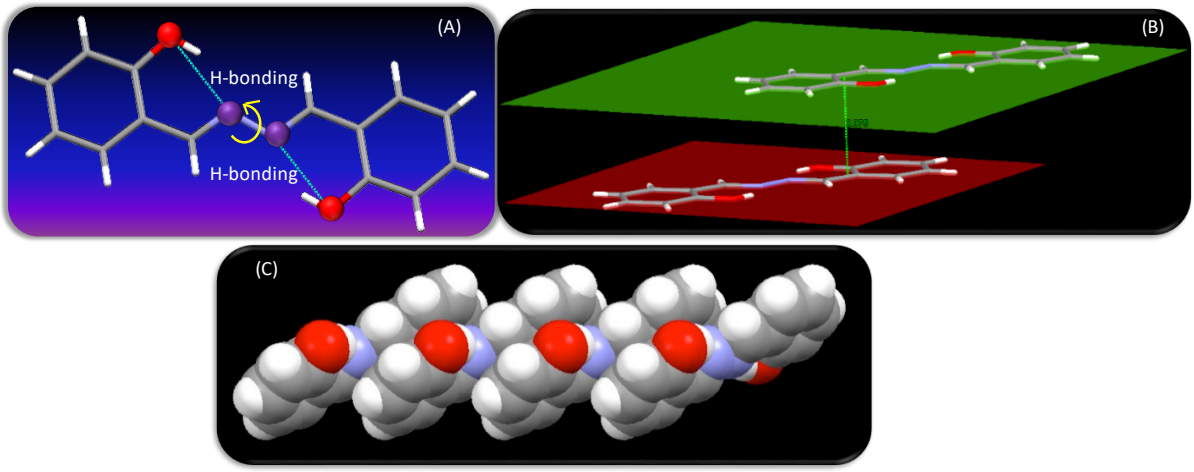


**Figure 2.21** (A) Capped sticks model of crystal **$H_2$SA** (obtained from 1/CsOH solution) demonstrate the H-bonding (2.612 Å), possibility of ESIPT phenomenon and rotation around N9-N9 bond, (B) Distance between planar surfaces of two molecules was accounted as 3.375 Å which falls in appropriate range of π–π stacking and (C) Crystal packing (spacefill model) shows possibility of π–π stacking which is in full agreement with the results obtained from dilution of gel in fluorescence experiment and Space fill model of crystal **$H_2$SA**/$Cs^+$.

## 2.9 RHEOLOGICAL STUDY

In order to support the true gel phase material, detailed dynamic rheological experiments were carried out with freshly prepared gel (1% w/v) and the results are shown in Fig 2.22. A stress sweep experiment (oscillation frequency 1 Hz at 25 $^{o}$C) shows that the storage modulus (G$^{'}$) is found to be approximately 1 order higher than that of the loss modulus (G$^{''}$) up to 1.5 Pa, above which deformation takes place and both the moduli cross each other at a certain point, 2.3 Pa, which indicates the soft-solid like characteristics of **$H_2$SA**/$Li^+$ containing metallogel. In a strain sweep experiment, at a constant oscillation frequency of 1 Hz, the gel was stable up to ~10% strain with a negligible effect over elasticity but further strain leads to the phase transition from gel to sol phase. Dynamic frequency sweep measurements show that G$^{'}$ and G$^{''}$ are linearly parallel to each other up to long range (0.75 to 1.6 rad $s^{-1}$) which supports the predominant elastic nature. G$^{'}$ and G$^{''}$ have been measured in the range 20–90 $^{o}$C at a constant frequency of 1 Hz strain. The metallogel shows nearly unchanged viscoelastic behavior from 20 to ~50$^{o}$C and started deformation above ~50 $^{o}$C, which is expected for a chloroform and methanol containing gel. Further, the sharp critical temperature ($T_{gel}$) was acquired from the derivative plot between loss tangent (tan $\delta$= G$^{''}$/G$^{'}$) and temperature, which confirms the $T_{gel}$ at 50 $^{o}$C. Further, the complex viscosity on the temperature ramp also supports the aforesaid critical temperature of the gel. Thus, the rheological characterization of the present gel suggests the formation of a typical 'soft-solid like' gel phase material.[25]

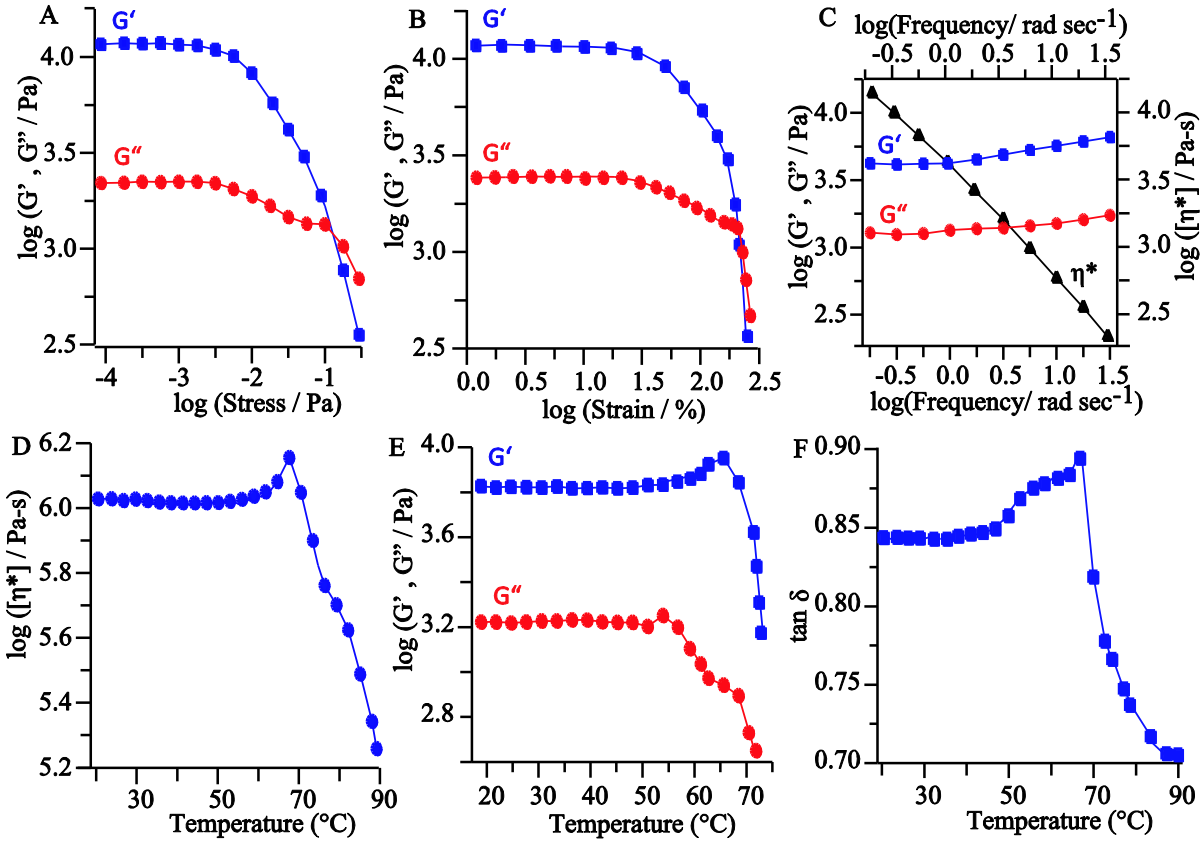


**Figure 2.22** (A) Dynamic shear stress of G' and G" at an oscillation frequency of 1 Hz at 25 °C, (B) dynamic oscillation strain sweep of G' and G" at a frequency of 10 rad $s^{-1}$ and temperature of 25 °C, (C) primary axis: dynamic frequency sweep measurements of G' and G" at a strain of 0.5%. Secondary axis: complex viscosity measurements, (D) dynamic temperature ramp of complex viscosity measurements at 5 °C $min^{-1}$, (E) dynamic temperature ramp G' and G" at a heating rate of 5 °C $min^{-1}$, strain of 0.5% and frequency of 10 rad $s^{1}$ and (F) dynamic temperature ramp of the loss tangent (tan $\delta$ = G"/G') plot at 5 °C $min^{-1}$ which indicates the phase transition temperature ($T_{gel}$) at ~70 °C.

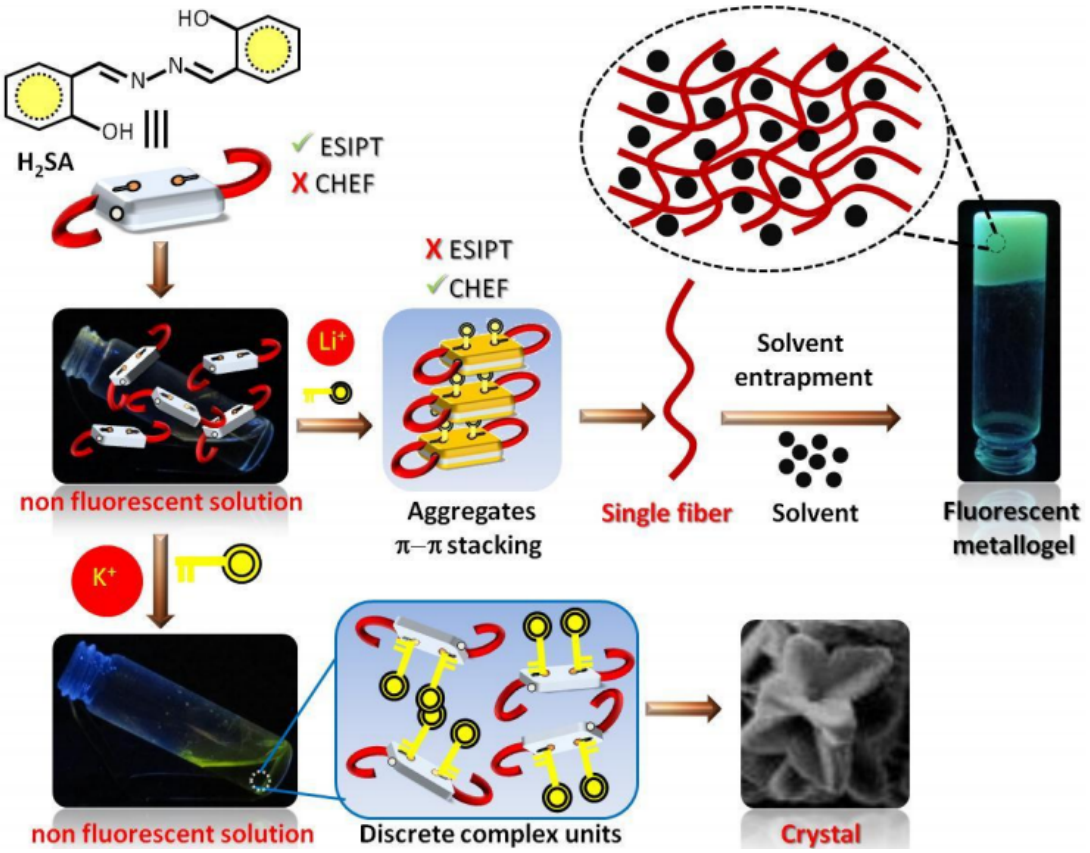


**Figure 2.23** A diagrammatic presentation of plausible mechanism behind metallogel formation.

## 2.10 CONCLUSION

In conclusion, through this chapter, we have described the synthesis and properties of a fluorescent metallogel obtained from non-fluorescent constituents *viz*. an ultra-low molecular weight symmetrical ligand **$H_2$SA** and LiOH. The metallogel showed multi-stimuli responsive behavior towards temperature, mechanical stimuli and ultrasound. The metallogel demonstrated the alkali metal size dependent morphological variance (fiber to crystal) as well as fluorescence properties. LiOH not only deprotonated **$H_2$SA** but also induced strong fluorescence through electrostatic interaction and inhibition of ESIPT lead to highly intense fluorescence due to occurrence of CHEF. Further, CHEF and π–π stacking played a crucial role in the appearance of fluorescence and metallogel formation. Moreover, the slight

variation in spacer and functional groups in such small systems result into gel/sol/ precipitate and the corresponding interesting phenomenon of ESIPT-CHEF to ICT. True gel phase material was attested by rheological studies. The present gel may find application in designing of other lower molecular weight gels and can be used for metal ion sensing.